Overcoming thermal instability of polymeric Core-Shell-Particles: Advanced processing options for the preparation of Stimuli-Responsive structural color materials

Lukas Siegwardt [a], Markus Gallei [a,b,*]

[a] *Polymer Chemistry, Saarland University, Campus C4 2, 66123 Saarbrücken, Germany*
[b] *Saarene, Saarland Center for Energy Materials and Sustainability, Campus C4 2, 66123 Saarbrücken, Germany*

A B S T R A C T

Core-shell particles (CSP) represent one of the most promising building blocks for the artificial production of stimuli-responsive materials with iridescent structural colors. Despite tremendous efforts in the past two decades, scalable processing options for CSP are overall rare and mostly limited to 2D structures in the form of films and foils. This work investigates why common large-scale polymer-processing techniques, such as injection molding or fused filament fabrication, are hardly applicable to state-of-the-art CSP: While rheological prerequisites are fulfilled, thermal stability is proven to be surprisingly poor. Temperature instability during processing is caused by a thermally induced cross-linking reaction of residual reactive moieties. This undesired cross-linking reaction can be efficiently suppressed via optimizations of the particle architecture, in terms of adjusting the core-to-shell ratio and number of grafting anchors. Thermal stability can be further increased upon incorporation of primary antioxidants. The theoretical framework and the feasibility of the developed solution strategies are verified by a variety of thermoanalytical methods, including differential scanning calorimetry, thermogravimetric analysis, as well as rheological and mechanical measurements. Finally, advanced CSP are developed and demonstrated to be conveniently processable at elevated temperatures of up to 250 °C. These next-generation CSP formulations are advantageous for established processing techniques and may further pave the way for the design of new large-scale methods suitable for industrial use. Potential applications are smart sensors, advanced display technologies, or anti-counterfeiting materials.

1. Introduction

Fascinating structural colors are commonly found in natural organisms such as butterflies [1], peacocks [2], or chameleons [3]. In contrast to colors derived by pigments or dye, wherein organic molecules or transition metal ions absorb a defined range of wavelengths, structural coloration arises from the interference of visible light with periodic structures on the nanometer length scale. The vivid structural colors do not rely on toxic ingredients and are not prone to photobleaching [4–6]. This eco-friendliness and fade-resistance make them promising candidates for anti-counterfeiting materials [7,8], smart sensors [9,10], optical coatings [11,12], and display technologies [13–15].

Despite tremendous efforts in artificially reproducing structural color, today's large-scale production in terms of bulk material fabrication is rare, as recently reviewed by Zhang et al. [16,17] and other

authors [18–23]. As periodic structures at a length scale of a few hundred nanometers are required, the self-assembly of building blocks that are already at this length scale simplifies the fabrication process [13,24,25]. Self-assembly approaches are further advantageous because of their low-cost building materials, convenient fabrication processes, and ease of scaling up [13]. One of the most promising building blocks for colloidal self-assembly are core–shell particles (CSP). The advantages of CSP are the tailorable and scalable synthesis [26], as well as the tunable mechanical and rheological properties [27,28]. Furthermore, CSP-based materials do not suffer from internal multiple scattering and the reflected wavelength does not interfere with the resonances of individual particles [20,29].

CSP are usually prepared via stepwise starved-feed emulsion polymerization protocols [26]. Obtained pure organic or hybrid particles consist of a rigid core onto which a softer shell is grafted, providing a

"gum-like" matrix [30]. Upon shearing at elevated temperatures during processing, the soft shell forms a coherent and viscous matrix around the non-deformable core particles, which self-assemble into long-range-ordered colloidal crystals. Thus, so-called *polymeric opals* are formed. For successful self-assembly, covalent grafting of the shell-polymer via a small interlayer between core and shell is mandatory to ensure the processing stability of CSP. Covalent linkages prevent detachment of the shell-polymer chains and phase separation of core and shell during particle processing [31–33]. The core particles often consist of cross-linked polystyrene, whereas the comparably soft shell usually consists of polyalkylacrylates [34–39]. Hybrid materials with inorganic cores [40,41] have also been exploited; as well as a variety of other shell materials, including sol – gel materials [42], metallopolymers [43,44], ceramic precursors [45–47], or biopolymers [48].

Due to periodical changes in the refractive index between core and shell, ordered CSP scatter light according to the Bragg-Snell-Law. The ordered structure is formed by the spherical core particles, surrounded by a continuous shell matrix. As the lattice constant in Bragg's Law is proportional to the particle diameter D and particle diameters can be adjusted easily, all colors of the rainbow can be achieved. Another interesting feature of CSP-based materials are their mechanochromic features, as the lattice constant – and therefore the reflected wavelength – changes upon mechanical deformation. The reflected color also depends on the angle of incident light, leading to an iridescent visual appearance [38,49–51]. By incorporation of stimuli-responsive (co) polymers, CSP-based materials can respond to external triggers with a reversible visual change. Feasible stimuli comprise, e.g., pH-value [35,52], electric or magnetic fields [43,44,53–55], solvents [56,57], and temperature [34,39,54,56].

Several self-assembly strategies have been developed to produce ordered colloidal crystals from CSP, which has recently been reviewed by Xiong [48] and other authors [14,26,58,59]. Most of the commonly applied methods rely on a substrate and a dispersion medium, e.g., spin-coating [60,61] or drying techniques [58,62]. Free-standing opal films are accessible with the melt-shear organization technique [32,33,63]. Fiber- [64] and foil-extrusion [30,31] have been conducted over dimensions of several meters with industrial-grade techniques. Most recently, CSP have also been 3D printed with a custom-built 3D printing system by our group [27]. However, CSP have never been processed into 3D bulk structures with industrial-suitable methods. Early attempts to process the material via compression- or injection molding were only briefly mentioned, never upscaled and limited to very rough and non-complex geometric shapes with a low degree of resolution [65,66]. To the best of our knowledge, other common polymer processing techniques have not been reported. This includes e.g., profile extrusion, melt casting, rotational molding, blow molding or parison forming, embossing, or fused filament fabrication and other commercialized 3D printing techniques.

All the above-mentioned industrial manufacturing techniques require a top-down approach where a particular macroscopic shape is given to the material. This must be combined with the bottom-up self-assembly, leading to a structural color [20]. In principle, CSP meet the rheological prerequisites [67,68], as the soft shell leads to a polymer-melt-like flow behavior at elevated temperatures [30,69,70]. Additionally, any type of directional shearing during processing should lead to self-assembly of the particles, as the colloidal crystalline order is thermodynamically favored [26,30,33,69]. Despite this huge potential, as of today scalable processing options are limited to films and foils. No large-scale processing technique for structurally colored 3D bulk structures has been realized that would be cost-effective enough to allow their widespread use [30].

In this work we demonstrate reasons and solutions to these issues: For the first time, we systematically investigate the thermal stability of CSP, evidencing that it is surprisingly poor and not sufficient for common polymer processing techniques. A variety of possible solutions are presented, thus paving the way to a new generation of CSP suitable for

the mass manufacture of polymeric opals.

2. Materials and methods

2.1. Materials

Styrene (S, 99 %) was purchased from Fisher Scientific. Butane-dioldiacrylate (BDDA, 90 %), methylmethacrylate (MMA, 99 %), and ethylacrylate (EA, 99.5 %) were purchased from Sigma-Aldrich. Allyl-methacrylate (ALMA, 98 %) was purchased from TCI. Before emulsion polymerization, radical inhibitors were removed from the monomers by passing them through a basic alumina column (50–200 μm, Acros Organics). Potassium hydroxide flakes (KOH, 90 % reagent grade), sodium disulfite (NaDS, analysis grade), sodium persulfate (NaPS, $\geq$ 98 %), and sodium dodecyl sulfate (SDS, $\geq$ 98.5 %) were purchased from Sigma-Aldrich. Dowfax2A1 was purchased from EZkem.

Carbon Black (Channel Type Black 4) was obtained from Evonik. BYK-MAX HS 4309 (HS4309) was obtained from BYK. Pentaerythritol-tetrakis(3-[3,5-di-*tert*-butyl-4-hydroxyphenyl]propionate) (AO1010) was obtained from Nordmann-Rassmann under the tradename *Norantox1010*. Benzene-1,4-diol (Quinol, 99.5 %) was purchased from Acros Organics.

2.2. Instrumentation

Dynamic light scattering (DLS) measurements were performed with a Zetasizer ZS 90 by Malvern Instruments equipped with a 4 mW, 633 nm HeNe Laser. All measurements were carried out at 25 °C and an angle of 90° with a five-fold determination of an automatically determined number of runs (typically 10–20 runs per measurement). Automated data acquisition in 300 size classes was carried out using a cumulant fit. The hydrodynamic diameter D_{DLS} represents the z-average of this fit, with the polydispersity index (PDI) as width parameter.

For transmission electron microscopy (TEM) studies, a diluted polymer dispersion was drop-casted on a carbon-coated copper grid. The dispersion medium evaporated at ambient conditions for 24 h. TEM experiments were conducted using a JEOL JEM-2100 electron microscope at a nominal acceleration voltage of 200 kV with a Gatan Orius SC100 CCD camera in bright field mode. For the determination of mean particle diameters D_{TEM}, 25 particles per image were analyzed using the software ImageJ. The coefficient of variation was calculated as standard deviation divided by mean particle diameter and is indicated with $\pm$. Scanning electron microscopy (SEM) was carried out on a Zeiss Gemini500 Sigma VP device using the software SmartSEM Version 6.07, with accelerating voltages between 2 and 4 kV.

Temperature-dependent (heating rate: 5 K min^{-1}) and isothermal rheological properties were determined with an Anton Paar MCR501 oscillatory rheometer at a frequency of 1 Hz using a 25 mm plate-plate geometry. Temperature-dependent (heating rate: 5 K min^{-1}) and isothermal differential scanning calorimetry (DSC) were carried out with a Netzsch 214 F1 Polyma. DSC measurements for comparative analysis of glass transitions were conducted with a heating rate of 10 K min^{-1}, as described in the respective figure legends. Temperature-dependent (heating rate: 10 K min^{-1}) and isothermal thermogravimetric analyses (TGA) were performed with a Netzsch TG 209 F1 Libra system. The heat flow during TGA measurements was recorded with calculated dynamic temperature analysis (c-DTA by Netzsch). IR spectroscopy was conducted with a Bruker Alpha II spectrometer.

Tensile tests were performed using a Zwick/Roell universal testing machine with a testing speed of 1.0 mm s^{-1} and the software testXpert II. Shore-D Hardness was determined using a Sauter HBD 100–0 Durometer.

Reflection spectra were recorded using an Ocean Optics fiber FLAME vis/NIR spectrometer USB2000 in reflection mode, combined with an Ocean Optics deuterium/tungsten halogen lamp DT mini 2. All spectra were calibrated with a diffuse white reflectance standard by Thorlabs

(PMR10P1). Calibrated intensities were normalized with respect to the highest intensity in the respective measurement series.

2.3. Synthesis and processing

The following protocol was used to synthesize batch CSP1. Syntheses of the other batches mainly followed this protocol, with minor adjustments which are described in the main text and the Supporting Information. A 5 L double-wall reactor under nitrogen atmosphere at 75 °C, equipped with a reflux condenser and a stirrer, was filled with a monomer emulsion (ME0) of 13.5 g S, 1.50 g BDDA, 0.812 g SDS, and 1050 g deionized water. While stirring at 250 rpm, the polymerization was initiated with 0.270 g NaDS and 1.95 g NaPS. After a reaction time of 10 min, a monomer emulsion (ME1) was added continuously with a flow rate of 2.7 mL min^{-1}, using a rotary piston pump (Ismatec reglo-CPF digital, RH00). ME1 contained 132 g S, 13.2 g BDDA, 0.433 g SDS, 0.752 g KOH, 0.414 g Dowfax2A1, and 169 g deionized water. After the complete addition of ME1, the reaction was kept at a constant temperature and stirred for 15 min. While stirring at 250 rpm, the polymerization was reinitiated by adding 1.00 g NaPS. After a reaction time of 15 min, a monomer emulsion (ME2) was continuously added with a constant flow rate of 5.0 mL min^{-1}. ME2 contained 17.8 g MMA, 1.78 g ALMA, 0.345 g Dowfax2A1, 0.174 g SDS, and 76.7 g deionized water. After the complete addition of ME2 and an additional 15 min, a monomer emulsion (ME3) was continuously added with a flow rate of 5.0 mL min^{-1} using a rotary piston pump. ME3 contained 219 g EA, 0.862 g SDS, 0.696 g Dowfax2A1, 1.21 g KOH, and 286 g deionized water. After the complete addition of ME3, the reaction mixture was kept at a constant temperature and stirred for an additional hour.

After synthesis, the emulsified particles were freeze-dried. The dried particle mass was mixed with 0.03 wt% Carbon Black and optionally an antioxidant, as described in the main text. The mixture was extruded with a Thermo Scientific HAAKE MiniLab 3 Micro-Compounder. Opal films were produced with the melt-shear technique: A 2 g portion of the extruded mass was covered with two polyethylene terephthalate (PET) foils (Mylar A75, DuPont) and inserted into a laboratory press (Collin P 300 E) for 3 min and 20 bar. Unless otherwise indicated, a temperature of 100 °C was used for extrusion and melt-shear processing. For 3D printing, the extruded mass was printed on a Saarpricom Delta UpSD 3D Printer, equipped with a 0.4 mm Nozzle. Slicing was performed with Simplify3D V4.1.2. Unless otherwise indicated, printing settings were used as described in a previously published slicing profile [27].

3. Results and discussion

3.1. Synthesis, Processing, and thermal instability of state-of-the-art particles

CSP have been synthesized by different groups from different disciplines [26,30,65,70,71]. Within this context, stimuli-responsiveness was implemented via copolymers in the shell material, and several types of additives were incorporated after synthesis. However, particle architecture and basic monomer composition were rarely altered. The common synthesis strategy to achieve this archetypal particle structure was also used in this work to synthesize the batch CSP1. Semi-continuous and stepwise emulsion polymerization was used for this purpose, as described in the following and illustrated in Fig. 1a.

In the first step, poly(styrene-*co*-butanedioldiacrylate) (P(S-*co*-BDDA)) core particles were synthesized. As given in Fig. 1b, the hydrodynamic diameter D_{DLS} of the core particles according to dynamic light scattering (DLS) was adjusted to 166 nm (PDI 0.039). BDDA was used as a chemical cross-linking reagent to avoid deformation of the core particles during subsequent processing. In the second step, an interlayer of approximately 3 nm ($D_{DLS} = 169$ nm; PDI 0.021), consisting of poly (methylmethacrylate-*co*-allylmethacrylate) (P(MMA-*co*-ALMA)) was introduced. As ALMA provides two different reactive sites, the soft polymer shell of polyethylacrylate (PEA) could be covalently anchored in the following step [72,73]. The final CSP were found to be
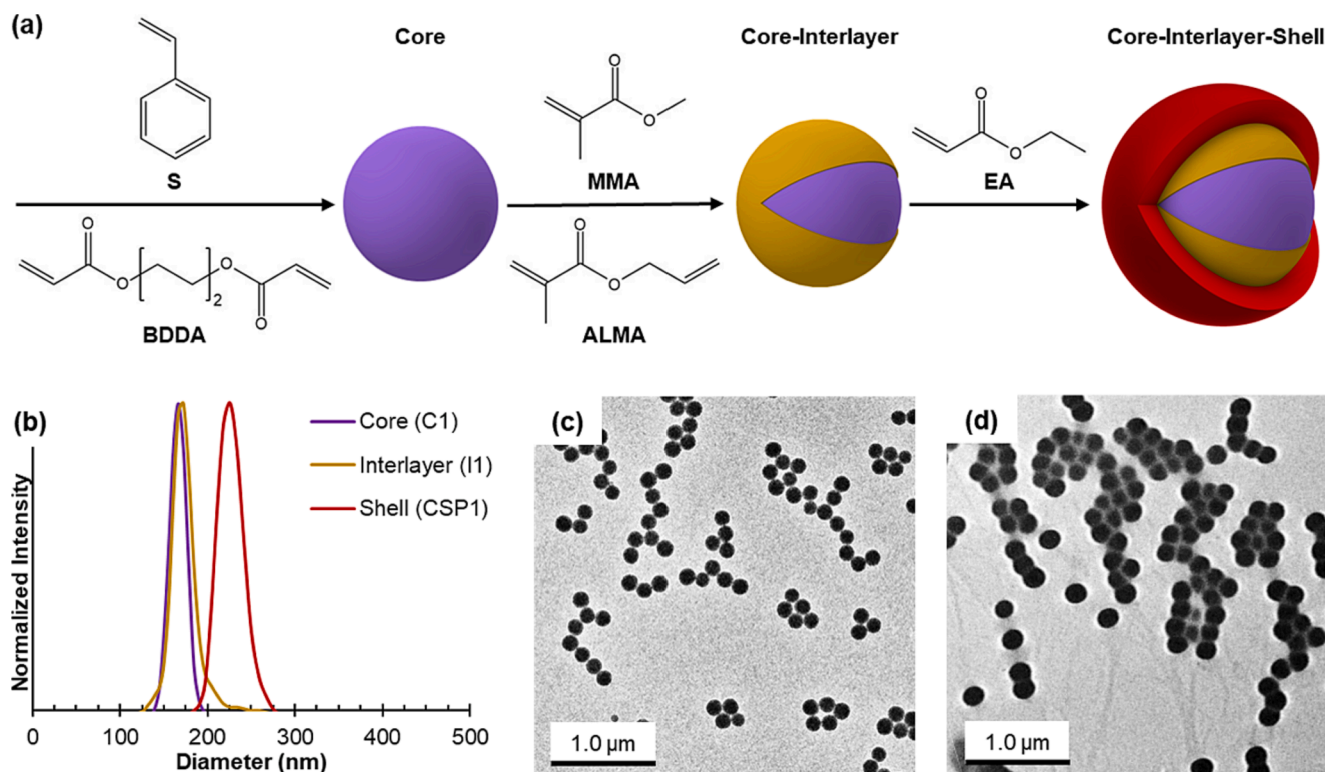
Fig. 1. A) Synthesis scheme for the preparation of CSP via semi-continuous starved-feed emulsion polymerization. **b)** DLS data of the particles for individual reaction steps. **c)** TEM photograph of the core particles. **d)** TEM photograph of the final CSP particles.

monodisperse with an average diameter of $D_{DLS} = 223$ nm (PDI 0.018).

In addition to DLS measurements, the particle size in the dried state D_{TEM} was determined using transmission electron microscopy (TEM). While DLS analysis determined the hydrodynamic diameter in a swollen state, TEM measurements revealed the average particle diameter in the dried state. From the corresponding TEM images in Fig. 1c and d, it can be concluded, that good control over the polymerization was achieved, resulting in an average core diameter of 157 nm (±4.0 %), an interlayer of 161 nm (±4.6 %) and finally monodisperse CSP of 205 nm (±4.4 %).

CSP are usually processed with special manufacturing techniques at elevated temperatures of 60–120 °C [26,30,31,39,56], occasionally up to 140–150 °C [27,55,71,74–76]. However, as described in the introduction, most common polymer-processing methods require much higher temperatures. High processing temperatures may also be favorable for established CSP-processing methods, regarding the increased flowability and therefore reduced extrusion force. While trying to process CSP1 at higher temperatures than previously reported via extrusion, 3D printing, or melt-shearing, the following recurring observations were made: The material got brittle and crumbly, processability worsened, structural color quality drastically decreased, surface roughness increased, multiple crack formation occurred, and only short coherent pieces could be produced before the structure broke or cracked. At temperatures of 180 °C and higher, the material became completely impossible to process via extrusion and 3D printing, in the form of exceeding the maximum extruder-torque and clogging the 3D printer's nozzle, respectively. The formation of an at least somewhat coherent film by application of the melt-shear technique was found to be impossible at temperatures above 200 °C. These observations were generally surprising, as polystyrene- and polyacrylate-based materials are commonly processed at temperatures in a range of 200–250 °C in industry [67,77]. It was therefore assumed that the thermal instability resulted from the particular core–shell architecture. The following chapter presents experimental proof for this hypothesis, followed by a discussion of the underlying mechanisms.
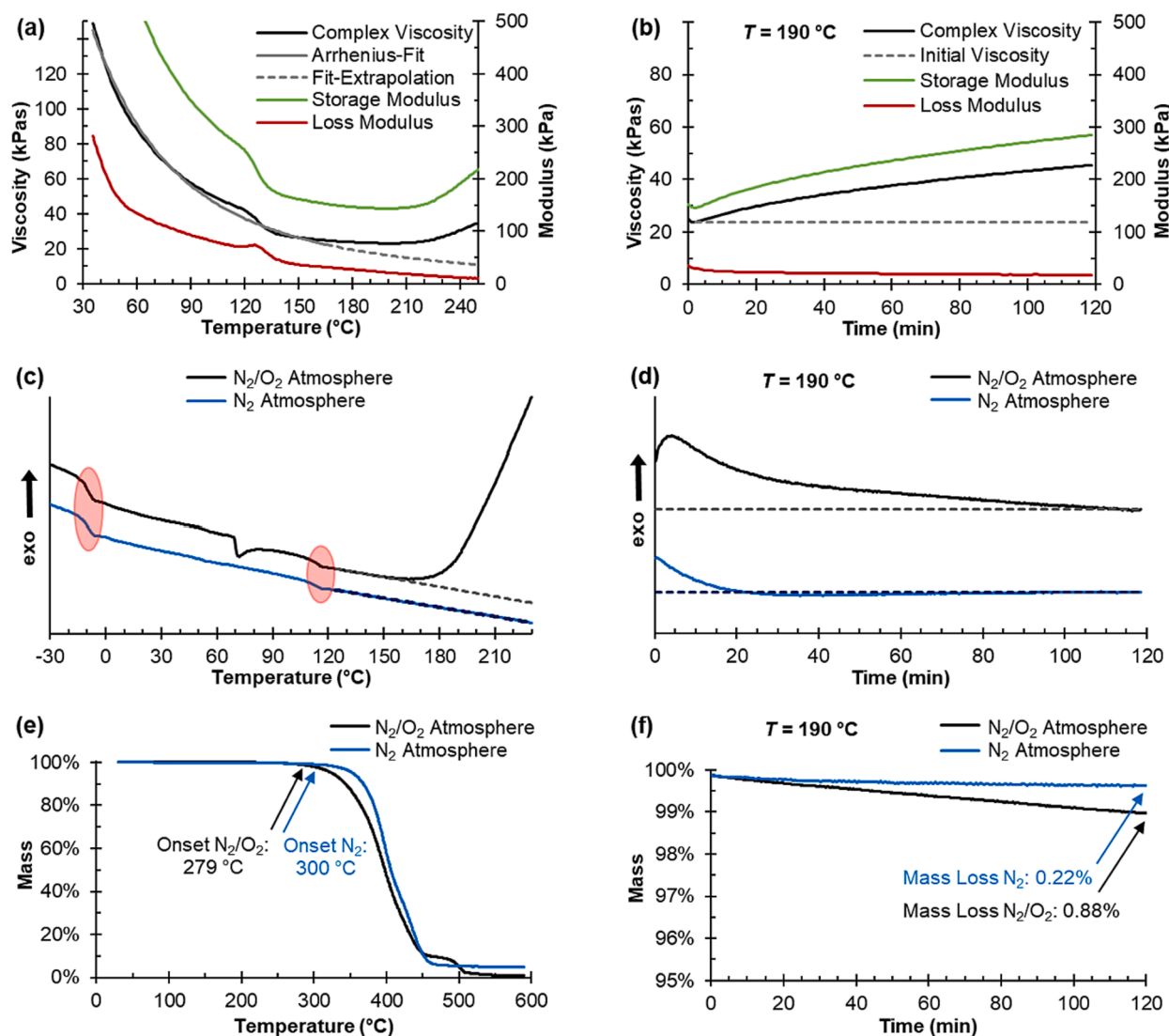
Fig. 2. Analysis of the temperature stability of CSP1. The left column shows temperature sweeps in different temperature ranges, while the right column shows data obtained from isothermal measurements at 190 °C for 120 min. **(a)** Temperature-dependent rheological measurements under ambient atmosphere. In a temperature range from 35 °C to 165 °C measured viscosities were fitted to an Arrhenius-Law and extrapolated for higher temperatures. **(b)** Isothermal rheological examination under ambient atmosphere. The minimum viscosity after a homogenous sample temperature of 190 °C was reached is sketched as a horizontal dotted line. **(c)** Temperature-dependent DSC measurements in N_2 and N_2/O_2. Glass transition temperatures are indicated with a red circle and the base signal without any endo- or exothermic process is represented by dotted lines. **(d)** Isothermal DSC thermograms in N_2 and N_2/O_2, wherein the base signal is represented by dotted lines. **(e)** Temperature-dependent TGA in N_2 and N_2/O_2. **(f)** Isothermal TGA in N_2 and N_2/O_2.

3.2. Mechanism of thermal instability

To gain insights into the mechanism of the temperature instability, we conducted in-depth analyses of particle batch CSP1. This batch represents the state-of-the-art particle architecture and composition for elastomeric opal film formation by application of the melt-shear organization technique [26,30,31]. Temperature-dependent rheological properties up to 150 °C of almost identical CSP have been previously investigated by Finlayson et al., revealing that the thermomechanical properties are mainly influenced by the elastomeric shell material [30,69]. In accordance with this reference, Fig. 2**a** shows how viscosity rapidly decreased upon heating from room temperature. The viscosity drop at 125 °C relates to the glass transition of the cross-linked core particles. Viscosity then asymptotically flattened off up to 165 °C, resembling the common thermorheological behavior of an elastomer with non-covalent physical cross-linking sites. An Arrhenius regression for the temperature-dependent viscosity $\eta(T)$ according to equation (1) was fitted to measured viscosities in a temperature range from 35 °C to 165 °C. Therein R is the universal gas constant and η_0 the reference viscosity at $T_0 = 150$ °C. E_A describes the activation energy, which was obtained as a fit parameter by minimizing the sum of squared errors. The chosen model is not able to account for the glass transition of the core particles but revealed a low mean deviation of 4.1 %. The rheology of the particles was thereby found to be predominantly governed by the viscoelastic nature of the shell quasi-matrix, confirming the findings made by Finlayson et al.

$$\eta(T) = \eta_0\, e^{\frac{E_A}{R}\left(\frac{1}{T} - \frac{1}{T_0}\right)} \tag{1}$$

Calculated viscosities for $T > 165$ °C are indicated as dotted line in Fig. 2**a** to visualize the divergence between expected and observed behavior. In a range from 165 to 210 °C, measured viscosities deviate from the calculated values, as they stay on a roughly constant level. At first glance, this may be interpreted as a rubbery plateau. Such plateaus are caused by polymer chain entanglements that act like temporary cross-links, starting at temperatures above the glass transition [67,68]. As the glass transition of the shell material is well below room temperature (Fig. 2**c**), an attributable rubbery plateau may be observable in this temperature range, but not at 165 °C. Therefore, the plateau would have to be caused by entanglements of the core polymer between separate particles. This appears highly unlikely, as the cores are thoroughly cross-linked and surrounded by covalently grafted shell-polymer.

At temperatures > 210 °C the measured viscosity even increased with increasing temperature, further deviating from the expected course. The rising complex viscosity was caused by an increase in storage modulus, whereas the loss modulus persistently decreased. This observation indicated a decrease in dissipative flow and an increasing elastic material behavior and stiffness upon temperature increase. The loss of the ability for viscous flow and plastic deformability was likely the cause for our phenomenological observations, since it impeded macroscopic malleability and microscopic self-assembly of the core particles into a colloidal crystalline structure. Therewith it was further confirmed that the previously observed stagnation was not caused by a rubbery plateau, but another phenomenon.

Similar results were obtained from an isothermal viscosity measurement for 120 min at 190 °C (Fig. 2**b**), wherein viscosity dropped initially and then asymptotically increased. The obtained curve shows similarities with a typical vulcanization curve [67,68]. The viscosity drop in the first few minutes is related to the heating phase of the rheometer furnace (it took 2–3 min to reach 190 °C) and a delay between device temperature and sample temperature (it took another 1–2 min until the sample with a thickness of 2 mm was homogenously heated). Within this time period, viscosity decreased with increasing sample temperature, which was to be expected from the previously investigated temperature-dependent rheological examination. The ensuing viscosity-

increase could be once again attributed to a rising storage modulus, whereas the loss modulus slightly decreased. Overall, viscosity increased by 91 % over two hours. It appears unlikely that the observed viscosity increase was a result of gelation or rheopexy. Such effects would at least partly be reversible, which does not fit our phenomenological observations. Moreover, CSP are known to be shear-thinning, not shear-thickening [27,30,70]. The isothermal characterization temperature of 190 °C represented a feasible compromise, since it was on the one hand high enough to examine the thermally induced process, but on the other hand low enough to avoid complete destruction of the sample due to said process and to avoid potential interference by other thermal degradation mechanisms.

To investigate the reaction enthalpy, differential scanning calorimetry (DSC) was conducted in a nitrogen (N_2) atmosphere as well as in a synthetic air (N_2/O_2) atmosphere (Fig. 2**c**). Both graphs featured glass transitions at −11 °C and 112 °C, which can be attributed to the shell and core, respectively. The presence of two glass transitions further proved the successful synthesis and the expected core–shell architecture. At higher temperatures, however, the course of the graphs differed. An exothermic peak with an oxidation induction temperature of 165 °C was observed under N_2/O_2, while no such peak appeared under N_2. The peak area of 69 J g^{-1} may be interpreted as the reaction enthalpy of the process, which led to the observed viscosity increase in Fig. 2a. The endothermic peak under N_2/O_2 at 70–80 °C could stem from the oxidation reaction of monomer residues or other reagents left from synthesis.

Fig. 2**d** shows an isothermal DSC measurement at 190 °C for 120 min. In contrast to the previously discussed DSC measurements, peaks were observed under both atmospheres. However, the peak area was one order of magnitude higher in N_2/O_2 (123 J g^{-1}) as in N_2 (14 J g^{-1}). Compared to Fig. 2**b**, the DSC curve resembles the first derivative of the viscosity curve and may therefore be interpreted as reaction enthalpy. Both DSC measurements showed that the investigated process is exothermic and vastly accelerated by the presence of oxygen. Therefore, mechanisms were taken out of consideration, that are endothermic or do not require oxygen, e.g. ceiling temperatures.

To analyze the thermal behavior further, we conducted thermogravimetric analysis (TGA) in N_2/O_2 and N_2. The temperature sweep (Fig. 2**e**) revealed degradation onsets of 279 °C (N_2/O_2) and 300 °C (N_2). Both onsets were found to be well above the previously investigated and herein relevant temperatures. This finding was further confirmed by the isothermal TGA measurement at 190 °C (Fig. 2**f**), illustrating that the mass loss after two hours was well below 1 wt%. These TGA proved that oxidative degradation processes or combustions do not contribute to the investigated process.

In summary of the presented first thermal investigations, we showed that the poor thermal stability of the CSP is related to the core–shell architecture and leads to an increase in viscosity and stiffness. The underlying mechanism was found to be exothermic, requires oxygen, and does not lead to a loss of polymer mass. This description is well-explainable by a subsequent chemical cross-linking process. Cross-linkable reactive sites were introduced by the incorporation of BDDA as a cross-linker for the core polymer and ALMA as a grafting anchor for the shell material. We assume, that thereby introduced double bonds were not quantitatively consumed during CSP synthesis. These non-consumed and chemically available reactive sites could lead to a subsequent cross-linking reaction at elevated temperatures > 165 °C. We assume that the cross-linking process follows a radical mechanism with oxygen-diradicals as initiators. A mechanism diagram of the cross-linking reaction and the chemical structure of the particles is provided in Figure SI 1.

Following this idea, thermal stability could be improved, if all cross-linking sites and grafting anchors were consumed during synthesis. Alternatively, oxygen radicals could be intercepted before initiation. A reduction of reactive cross-linking sites may be achieved by increasing the amount of shell material during synthesis or a reduction of grafting

anchors in the interlayer, while oxygen radicals could be intercepted by the incorporation of antioxidative additives after synthesis. These potential solutions are summarized in Fig. 3. In the following chapters, we will demonstrate that all three solutions can be successfully applied, thereby strengthening the proposed theoretical framework.

3.3. Optimizing the Core-to-Shell ratio

Thermal stability could be increased by consuming as many cross-linking sites and grafting anchors as possible during particle synthesis. One approach to achieve this goal was to increase the amount of soft shell material in the last polymerization step. Because of the grafting-through nature of the shell polymerization step, it appears likely that the more monomer is fed to the particles, the more grafting anchors should be consumed. Moreover, the shell-polymer acts as a spacer between reactive sites for interparticle cross-linking reactions. Common CSP used in shear-induced self-assembly usually feature core fractions of around 50 vol% [26,28,30,75].

For this purpose, four batches of CSP2.1 to CSP2.4 with different core-to-shell ratios were synthesized. We used the identical batch of core particles C2 for all four CSP, to directly compare the influence of the shell material. The average diameter of C2 was found to be $D_{DLS} = 177$ nm (PDI 0.036) and $D_{TEM} = 153$ nm (± 4.3 %). Starting from CSP2.1, the proportion of shell-forming monomer emulsion in starved feed mode was increased for each batch. Detailed synthesis protocols are compiled in the SI (Tables SI 1 and SI 2). CSP diameters were determined via TEM and DLS (Table 1). Since all batches featured an identical core size, particle sizes increased with higher shell-/lower core proportion. More detailed DLS- and TEM data are given in the SI (Figures SI 2 and SI 3). DSC measurements (Figure SI 4a) revealed similar glass transitions for all batches of -10 ± 1 °C (PEA shell) and 111 ± 1 °C (cross-linked PS core), thus confirming the success of the synthesis and the comparability of the batches. IR spectra in Figure SI 4b and the corresponding evaluation in Table SI 3 further indicated that the core proportion of the final particles continuously decreased from CSP2.1 to CSP2.4. Apart from expectable differences, which were caused by the different core-to-shell ratios, the IR spectra of the CSP were found to be almost identical, thus proving the good comparability of the synthesized batches.

Fig. 4a displays how viscosities increased at temperatures > 165 °C, although the fitted Arrhenius-Laws (dotted lines) predicted a further decrease. CSP2.1 with the highest core proportion revealed the strongest deviation, whereas CSP2.4 with the lowest core proportion showed almost no deviation. Similar observations could be made of the

Table 1

Overview of synthesized CSP to investigate the influence of the core-to-shell ratio.

Batch	D_{DLS} (nm)	D_{TEM} (nm)	Core Proportion
CSP2.1	213 PDI 0.039	181 ± 2.6 %	61 vol%
CSP2.2	233 PDI 0.025	202 ± 4.5 %	44 vol%
CSP2.3	252 PDI 0.019	217 ± 4.2 %	36 vol%
CSP2.4	271 PDI 0.033	224 ± 4.5 %	32 vol%

The hydrodynamic diameter in the swollen state was determined via DLS measurements. The TEM diameter represents the size of the dried particles. The volumetric core proportion was calculated according to TEM Data.

isothermal viscosity measurement (Fig. 4b): the lower the core proportion, the lower the increase in viscosity. DSC measurements in Fig. 4c and d further verified this result, as the exothermic signal decreased upon reduction of the core proportion.

A summary of the rheological examinations and DSC measurements is provided in Fig. 4e, wherein integrated areas between expected and measured values are sketched against the core proportion. Integrated viscosities and enthalpies were connected with a linear fit, to visualize the decrease at lower core proportion. Therewith, it was demonstrated that the proposed solution approach worked: Remaining cross-linking sites were indeed reducible via a reduction of the core proportion, leading to enhanced thermal stability.

In analogy to CSP1, temperature-dependent and isothermal TGA measurements in N_2/O_2 were conducted for all particle batches CSP2.1 to 2.4. Results are illustrated in Figures SI 4c and d. In accordance with previous measurements, thermal degradation started well above 250 °C for all batches, and the average mass loss after 120 min at 190 °C was < 1.0 wt%. Once again it was thereby proven that oxidative degradation processes did not contribute to the investigated phenomena.

A lower proportion of the hard PS cores also led to an overall lower viscosity. This was expected, as the amount of low viscous shell-polymer was higher. Lower viscosities may be helpful for processing, in terms of increased flowability, but are not advantageous in general. Therefore, alterations of the general viscosity level are neither an argument for nor against low core proportions within the scope of this work. Besides, rheo-mechanical properties are easily tunable in a wide range without sacrificing color quality with co-monomers in the shell-polymer or incorporation of additives [27,28].

Opal films of all particle batches were prepared by application of the melt-shearing technique. The resulting films, as shown in Figure SI 5, were analyzed via reflection spectroscopy measurements in the visible range. The red-shift of the peaks in Fig. 4f from CSP2.1 to 2.4 resulted from the larger particle sizes (Table 1), which is in good accordance with Bragg's law of diffraction. CSP2.1 and CSP2.2 showed the same relative reflection intensity, which was used as a reference value of 100 % for this measurement series. For CSP2.3 and CSP2.4, relative reflection intensities were reduced to 73 % and 39 %, respectively. Moreover, peak sharpness decreased for CSP2.3 and CSP2.4, which may be interpreted as a decrease in color saturation. The reduced reflection intensity and color saturation are also visually observable in the photographs of the opal films made of CSP2.3 and 2.4, which barely show a defined reflection color at all. In summary, a reduction of the core proportion below 40 vol% led to a loss of structural color quality and should thus be avoided. An explanation is known from the literature: If the proportion of soft shell-material is too high, the self-assembly of the cores into a colloidal crystalline structure is impeded because of the increased space between individual core particles [26,28].

The influence of the core-to-shell ratio on mechanical properties is summarized in Figure SI 4e and f. Several systematic trends were observed. Tensile strength, stiffness (Young's Modulus) and hardness (Shore D) increased with the core proportion. The elongation at break on the other hand massively decreased with the core proportion from > 250 % for CSP2.3 and CSP2.4 over roughly 150 % for CSP2.2 to < 5 %
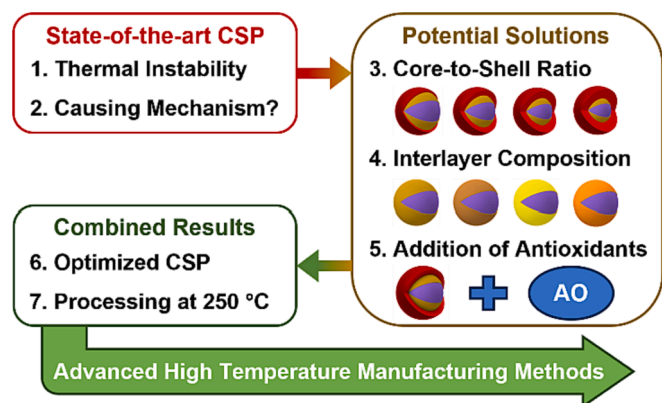
Fig. 3. Scheme of the applied strategies in this work. Within the first two chapters, a thermal instability issue was identified, and the underlying mechanism was elucidated. Thereof based solution approaches were tested in the following chapters 3.3 to 3.5. Finally, all solution approaches were combined, to synthesize and process a batch of optimized CSP in chapters 3.6 and 3.7. Advanced optical, thermal, and mechanical properties of the optimized batch are presented in chapter 3.8, thus illustrating application potentials.
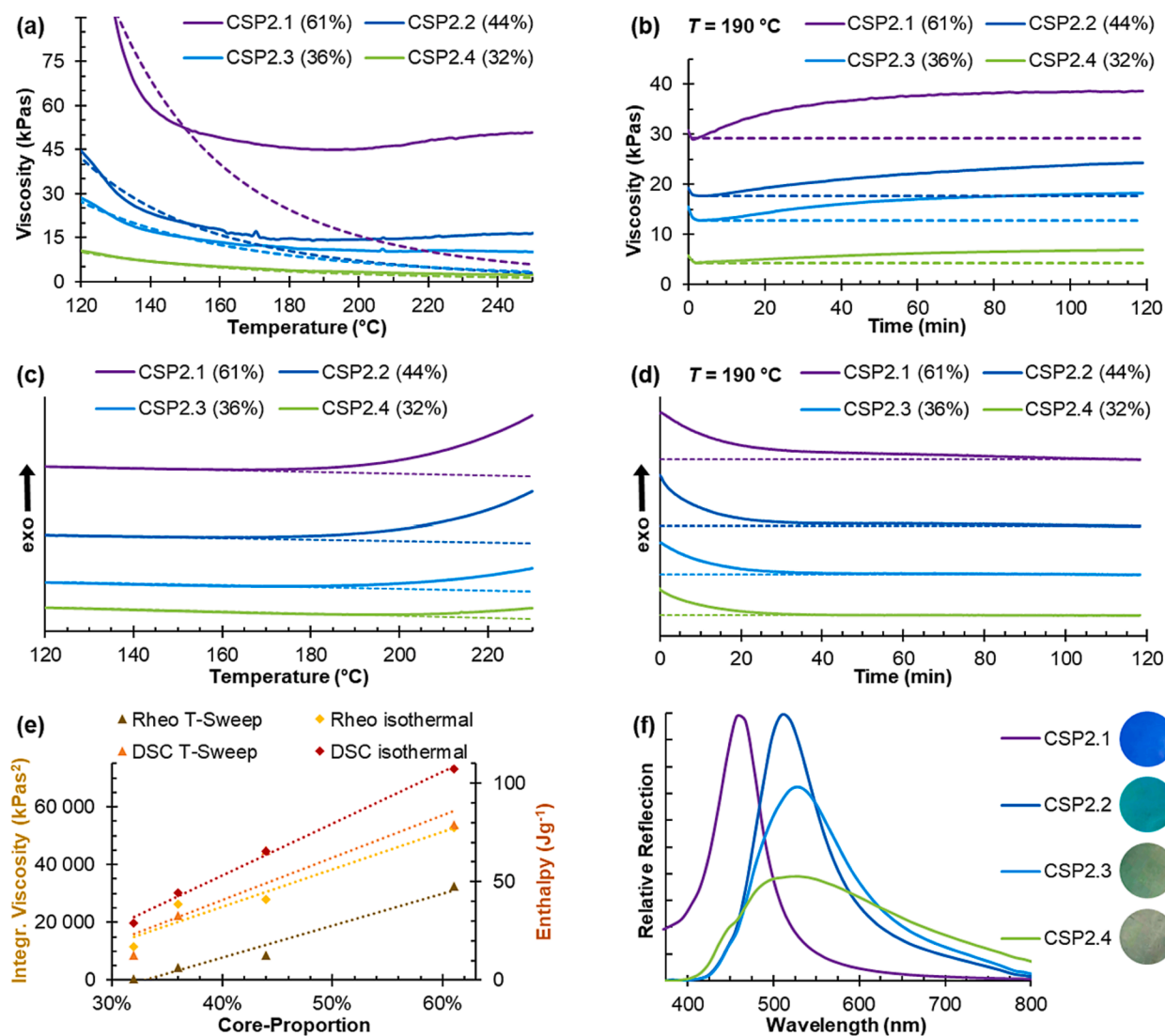
Fig. 4. Analysis of the temperature stability of CSP with different core-to-shell proportions. The core proportion according to TEM measurements is depicted in brackets behind the respective batch. **(a)** Temperature-dependent rheological examinations in ambient atmosphere in terms of dynamic complex viscosities. In a temperature range from 35 °C to 165 °C measured viscosities were fitted to Arrhenius-Law and extrapolated for temperatures > 165 °C. **(b)** Isothermal rheological examinations in ambient atmosphere. The minimum viscosity after a homogenous sample temperature of 190 °C was reached is sketched as a horizontal dotted line. **(c-d)** Temperature-dependent and isothermal DSC measurement in N_2/O_2, wherein the base signal is represented by dotted lines. **(e)** Summary of the measurements, sketched against the core proportion. For all four measurements, the area between the expected course and measured values was integrated with respect to the exposition time. **(f)** Reflection spectra of opal films, which were prepared via application of the melt-shear technique. The color of the opal film is shown as circles next to the figure legend.

for CSP2.1. All trends were expected, given the high stiffness and rigidity of the cross-linked core particles in contrast to the soft elastomeric shell. Only in case of CSP2.1, with a core proportion of 61 vol% a brittle fracture pattern was observed, whereas the other batches with a core proportion < 50 vol% showed ductile fracture, strong necking, and high stretchability. We assume that in case of CSP2.1, the comparably low amount of shell-polymer did not form a fully continuous matrix around the core particles. In this case, contacts between core particles would have led to crack formation at low strains, due to the non-deformability of the pristine cores. For the majority of applications for CSP, such as sensing or anti-counterfeiting, high elasticity and toughness can be considered more important than high strength and stiffness. It therefore appears advantageous to avoid high core proportions in order to achieve ductile-elastic material behavior instead of brittle fracture at low strains.

In conclusion of this chapter, a target of a core proportion of 40–45 vol% was found to be favorable to optimize temperature stability and mechanical properties while maintaining high structural color quality.

CSP2.2 featured this optimized core proportion, but still showed some cross-linking at elevated temperatures. Therefore, two additional solution approaches for overcoming this issue were exploited and will be presented in the following chapters.

3.4. Optimizing grafting properties

It is well known that the shell-polymer must be covalently grafted to the core to obtain an ordered colloidal crystal structure, which leads to the appearance of structural color [26]. Both stretching and compression are entropically unfavorable for the shell-polymer chains, which is why the grafted chains move the cores back to their lattice locations. Without sufficient grafting, the elastomeric matrix represents a highly viscous fluid, wherein the dispersed nuclei can be arbitrarily moved around. Usually, an amount of 10–15 wt% ALMA in the interlayer is used for this purpose [26,28,38]. If it were possible to reduce the amount of ALMA, while still ensuring that the shell-polymer was sufficiently grafted onto

the core, the number of unconsumed grafting anchors after synthesis could be reduced. As unconsumed grafting anchors act as reactive cross-linking sites during processing, a reduced amount would increase thermal stability.

To investigate this approach, four batches CSP3.1 to CSP3.4 with different amounts of ALMA in the interlayer were synthesized. Detailed synthesis protocols can be found in the SI (Table SI 1 and SI 4). The same batch of core particles (C3) was used for all four CSP, to improve comparability. The average diameter of C3 was determined as $D_{DLS} =$ 198 nm (PDI 0.039) and $D_{TEM} =$ 178 nm (± 3.6 %). The average particle diameters of the CSP were found to be very similar and are listed in Table 2, while more detailed data on particle size is presented in the SI (Figures SI 6 and 7).

DSC measurements (Figure SI 8a) revealed similar glass transitions for all batches of -10 ± 1 °C (PEA shell) and 112 ± 1 °C (cross-linked PS core), thus confirming the successful formation of the core–shell architecture and comparability of the batches. IR spectra in Figure SI 8b and the corresponding evaluation in Table SI 3 further indicated the good comparability of the synthesized batches. The spectra of the CSP differ only slightly in peak intensities, which can be attributed to minor differences in the core-to-shell ratio as obtained from DLS and TEM measurements: The lower the overall particle-size, the lower the shell proportion and the lower the intensities of peaks related to PEA as shell-polymer, relative to the intensities of peaks related to the PS cores.

Fig. 5a illustrates how viscosities increased at elevated temperatures, although the fitted Arrhenius-Laws (dotted lines) predicted a further decrease. The amount of deviation decreased at lower ALMA content, presumably due to a reduced amount of thermally induced cross-linking reactions. This observation was verified by isothermal viscosity measurements (Fig. 5b): A lower ALMA content once again led to a lower increase in viscosity. In isothermal mode, the viscosity curve associated with CSP3.4 showed an unusual progression. After the initial drop upon heating to 190 °C, viscosity did not increase immediately but stayed at a relatively constant level for roughly 30 min. This indicated that the thermally induced cross-linking reaction was decelerated and almost fully suppressed by reducing the ALMA content to 2.5 wt%.

Temperature-dependent and isothermal DSC measurements (Fig. 5c and d) further supported the results obtained from rheological examinations. The exothermic peak steadily decreased upon ALMA reduction. In the temperature-sweep, CSP3.4 showed an extraordinarily small signal, which even diminished at higher temperatures. In analogy to the viscosity measurements, this confirmed that cross-linking reactions were almost fully suppressed for this batch.

A summary of the four discussed measurements in terms of the integrated areas between expected and measured values is provided in Fig. 5e. Lower values indicate less thermally induced cross-linking reactions and thus higher thermal stability. Obtained values were connected with a linear fit to demonstrate the steady decrease upon reduction of ALMA. The achieved results proved that the amount of cross-linking reactions could indeed be suppressed via a reduction of the amount of ALMA, thus confirming the proposed solution approach. By reducing the ALMA content to very low levels thermally induced cross-linking reactions appeared to be almost fully suppressed. It is therefore likely that most of the cross-linking reactions are caused by unconsumed

reactive sites of ALMA during synthesis, whereas unconsumed BDDA moieties only play a minor role. This finding is in good accordance with literature, since cross-linking via allylic moieties of ALMA after synthesis has been observed before for PALMA-copolymers with PMMA and PS by Schmidt-Naake et al. [73]. Similar to the findings in this work, the authors report exothermic peaks and increasing viscosities in a temperature range from 160 to 250 °C, which are accelerated by oxygen and increase at higher ALMA-content in the copolymers.

A lower proportion of ALMA also led to an overall lower viscosity. As discussed above, this is neither an advantage nor a downside in general. However, it allows for gaining further insights into the particle architecture: ALMA acts as a grafting anchor for the shell, but not as a cross-linker between separate shell-polymer chains [26]. The increase in viscosity with higher ALMA content is therefore not assignable to a higher cross-linking density of the shell in general. It is rather likely that single shell-polymer chains were grafted to the core at several sites, which was enabled by the grafting-through nature of the polymerization. At higher ALMA contents, shell-polymer chains were increasingly often grafted to the core, thus reducing chain flexibility, which led to the observed increase in viscosity.

Temperature-dependent and isothermal TGA measurements in N_2/O_2 were conducted for all particle batches CSP3.1 to 3.4 (Figures SI 8c and d). Analogous to previous measurements, thermal degradation started well above 250 °C for all batches, and the average mass loss after 120 min at 190 °C was < 1.0 wt%. It was thereby once again verified that oxidative degradation processes did not contribute to the thermal instability of CSP.

To overcome the thermal instability of CSP-based materials, the ALMA content should be reduced as much as possible, while still ensuring that every chain of shell-polymer is covalently grafted to the core. Insufficient grafting would lead to a loss of structural color quality. To investigate this issue, opal films were prepared via the application of the melt-shearing technique and investigated with reflection spectroscopy measurements in the visible range. Photographs of the films are shown in Figure SI 9. The reflection spectra in Fig. 5f indicate that a reduction from the regular 10 wt% to 7.5 wt% or 5 wt% was possible with minor changes regarding color quality. CSP3.1 showed the highest reflection intensity and was thus used as reference with a relative intensity of 100 %. The relative reflection intensities were found to be at a comparably high level of 98 % for CSP3.2 and 95 % for CSP3.3. Peak sharpness, which may be interpreted as an indicator for color saturation, also remained unchanged. On a side note, the opal film made from CSP3.3 revealed a visible and measurable blue-shift of the color, by Bragg's law due to the comparably smaller particle diameter. Upon reduction to 2.5 wt% ALMA for CSP3.4, structural color quality decreased, in terms of relative intensity (64 %), peak sharpness, and visually perceived color. This indicated the presence of non-grafted polymer chains, interfering with the colloidal order of the core particles.

The influence of alterations in the amount of ALMA in the interlayer on mechanical properties is summarized in Figure SI 8e and f. During tensile tests, all samples showed brittle fracture. As discussed in chapter 3.3, this was likely the result of the comparably high core proportion of 55 vol% on average, which is on the upper end of the usual core fractions for state-of-the-art particles. However, several systematic trends were observed. On the one hand, tensile strength as well as elongation at break increased upon reduction of the ALMA-content. Samples with lower grafting-density were less susceptible to the brittle fracture pattern, presumably due to a higher grade of entanglements between shell-polymer chains. Moreover, the higher degree of freedom for the shell-polymer chains may have also led to a more extensive covering of the core particles, thus preventing core-core contacts, which are likely to facilitate crack-formation or -propagation and ultimately lead to the observed brittle fracture. On the other hand, Young's Modulus and Shore D-Hardness increased with increasing ALMA-content. This can also be explained by the increased grafting-density at higher ALMA-proportion, which leads to decreased mobility for the polymer chains

Table 2
Overview of synthesized CSP to investigate the influence of the interlayer composition.

Batch	ALMA Content	D_{DLS} (nm)	D_{TEM} (nm)
CSP3.1	10.0 wt%	252 PDI 0.032	224 $\pm$ 4.1 %
CSP3.2	7.5 wt%	247 PDI 0.018	216 $\pm$ 4.8 %
CSP3.3	5.0 wt%	239 PDI 0.029	215 $\pm$ 4.6 %
CSP3.4	2.5 wt%	243 PDI 0.022	218 $\pm$ 5.0 %

The hydrodynamic diameter in the swollen state was determined via DLS measurements. The TEM diameter represents the size of the dried particles.
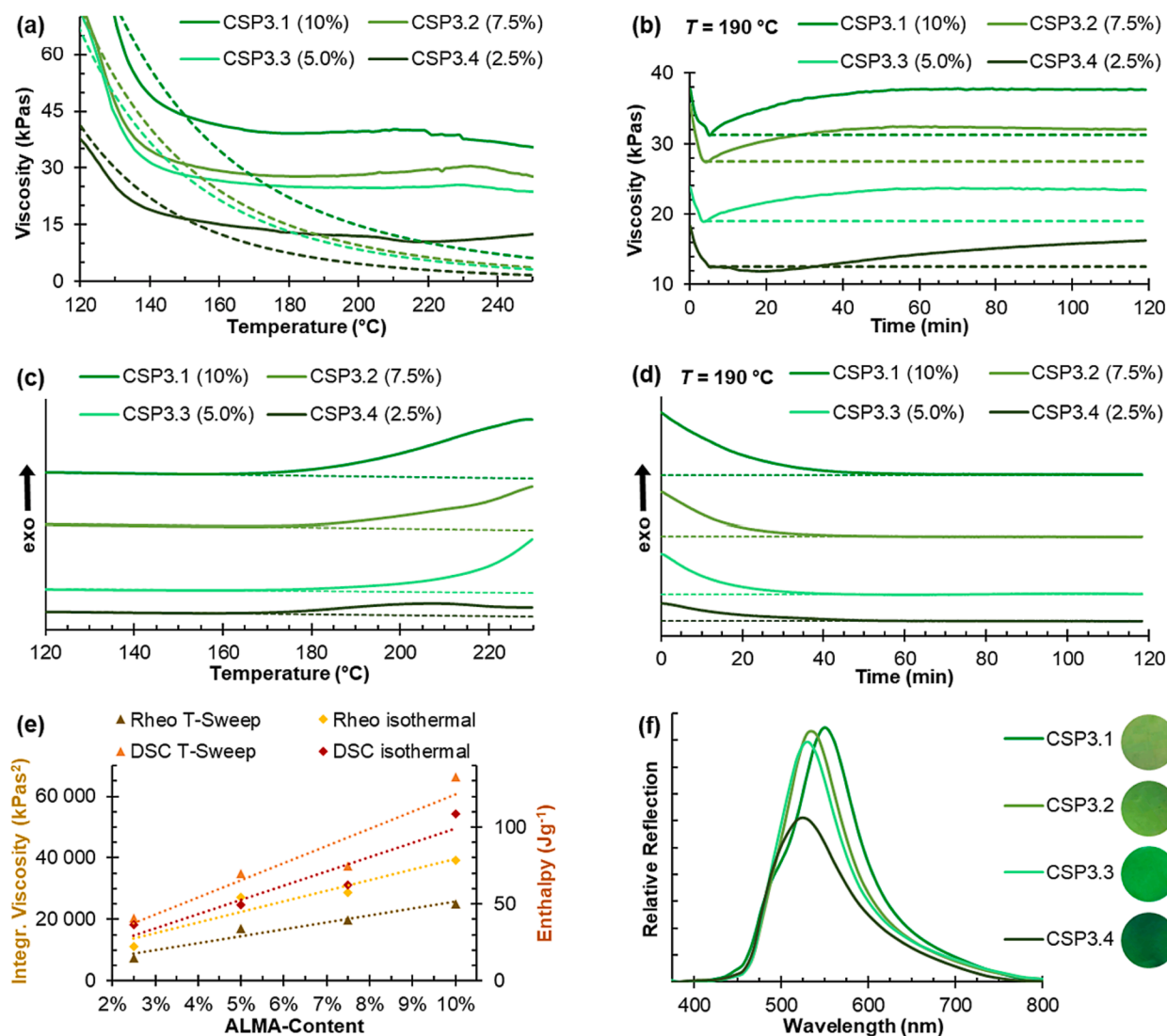
Fig. 5. Analysis of the temperature stability of CSP with different ALMA content in the interlayer. The ALMA content is depicted in brackets behind the respective batch. **(a)** Temperature-dependent rheological examinations in ambient atmosphere in terms of dynamic complex viscosities. In a temperature range from 35 °C to 165 °C measured viscosities were fitted to Arrhenius-Law and extrapolated for temperatures > 165 °C. **(b)** Isothermal rheological examinations in ambient atmosphere. The minimum viscosity after a homogenous sample temperature of 190 °C was reached is sketched as a horizontal dotted line. **(c-d)** Temperature-dependent and isothermal DSC measurements in N_2/O_2, wherein the base signals are represented by dotted lines. **(e)** Summary of the measurements, given against the ALMA content. For all four measurements, the area between the expected course and measured values was integrated with respect to the exposition time. **(f)** Reflection spectra of opal films, which were prepared via application of the melt-shear technique. The color of the opal film is shown as circles next to the figure legend.

in the soft shell matrix and thus a higher stiffness and hardness. Given the improved fracture resistance, a reduction of the ALMA-content below the state-of-the-art value of 10 wt% appears favorable.

In conclusion of this chapter, it is recommendable to decrease the amount of ALMA to ≈ 5 wt% to improve thermal stability and mechanical properties, while maintaining high structural color quality. Analogous to the first solution approach discussed in chapter 3.3, the thermally induced cross-linking reaction could be reduced, but not be fully suppressed. We therefore present an additional third solution approach in the following chapter to gain access to elastomeric opal structures with improved thermal stability and high color quality.

3.5. Antioxidative additives

The previously presented solutions aimed to reduce the number of reactive moieties in the polymerized particles, thus preventing subsequent cross-linking reactions. Another possibility could be to intercept initiating oxygen diradicals and propagating radicals with the use of antioxidants. Antioxidants are commonly used to retard the reaction of organic materials with atmospheric oxygen. Primary antioxidants act as free-radical scavengers, thereby significantly delaying or preventing oxidation. Secondary antioxidants decompose reactive hydroperoxides into thermally stable products and thereby stop chain branching. Primary and secondary additives are often used in combination for synergistic stabilization effects [78,79].

Within this work, we tested three different antioxidant formulations. All additives were incorporated in batch CSP1 via microextrusion with a proportion of 2 wt%. BYK-MAX HS 4309 (HS4309) is a commercial mixture of synergistic primary and secondary antioxidants, which are especially effective in styrene-based polymers. Benzene-1,4-diol (Quinol) is a common radical scavenger and a typical polymerization inhibitor for radical-initiated polymerizations. Pentaerythritol-tetrakis (3-(3,5-di-*tert*-butyl-4-hydroxyphenyl)propionate) (AO1010) is one of the most used sterically hindered phenolic antioxidants and commercially available as *Irganox1010* or *Norantox1010* [79].

The temperature-dependent viscosity of the compounds is illustrated

in Fig. 6a. While no antioxidant seems to be able to fully suppress the thermally induced cross-linking reaction, the increases in viscosity were not as distinct as for the raw polymer CSP1. The inhibiting effect of all three additives was even more pronounced for the isothermal measurement at 190 °C (Fig. 6b). Especially HS4309 and AO1010 vastly lowered speed and amount of the viscosity increase. The incorporation of quinol also led to an improvement, although less pronounced compared to the other additives. The improvements are most likely caused by decelerating and preventing thermally induced cross-linking reactions.

The overall level of viscosity increased upon incorporation of HS4309 and AO1010. Both additives seem to have acted as a thickening agent. Generally speaking, this is neither an advantage nor a downside, as discussed above. On the other hand, it indicated that the additives hinder particle motion, which may have an impact on the self-assembly process and thereof resulting structural color, as discussed later in this chapter. Such hindering of particle motion and impeding of chain entanglement has already been observed upon the incorporation of

similar concentrations of other low molecular additives [28].

Temperature-dependent and isothermal DSC measurements (Fig. 6c and d) supported the previous findings. Exothermic signals, related to thermally induced cross-linking, were reduced upon antioxidant incorporation. The graphs associated with additive-containing CSP are roughly comparable to measurements under N_2 (Fig. 2c and d). The isothermal DSC of the quinol compound showed a peculiarity in the form of a secondary peak after 75 min. Up to this point, all quinol could have been consumed, and the thermally induced cross-linking may have occurred. In accordance with this thesis, the secondary peak area and shape are very similar to the measurement of CSP1. Curves related to HS4309 and AO1010 did not show such a secondary peak, indicating that they were not fully consumed during the experimental period of 120 min. This observation fits the viscosity measurements, wherein the incorporation of quinol showed an improvement, but not as strong as the other two additives. However, DSC analysis must be interpreted with care. The physical and chemical properties of the additives as well as their antioxidative action may have led to additional exo- or
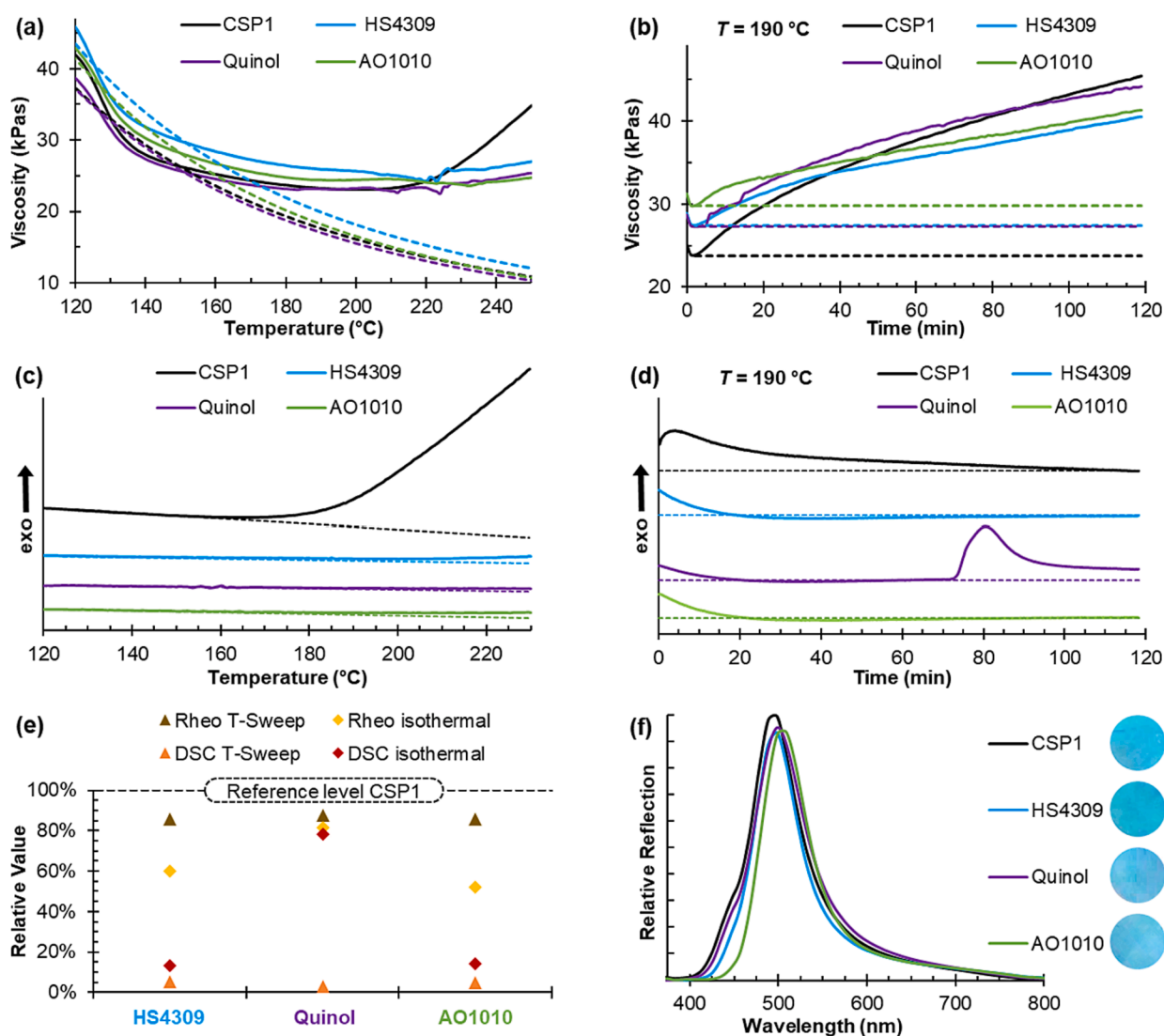
Fig. 6. Analysis of the temperature stability of CSP with different antioxidative stabilizers. CSP1 represents the original batch, without additives. **(a)** Temperature-dependent rheological examinations in ambient atmosphere in terms of dynamic complex viscosities. In a temperature range from 35 °C to 165 °C measured viscosities were fitted to Arrhenius-Law and extrapolated for temperatures > 165 °C. **(b)** Isothermal rheological examinations in ambient atmosphere. The minimum viscosity after a homogenous sample temperature of 190 °C was reached is sketched as a horizontal dotted line. **(c-d)** Temperature-dependent and isothermal DSC measurement in N_2/O_2, wherein the base signals are represented by dotted lines. **(e)** Summary of the measurements on stabilized batches. The areas between the expected courses and measured values were integrated with respect to the exposition time and normalized in relation to the original batch CSP1. **(f)** Reflection spectra of opal films, which were prepared via application of the melt-shear technique. The color of the opal film is shown as circles next to the figure legend.

endothermic signals, that could have superimposed the original signals. This was e.g. visible in the temperature-dependent DSC thermogram of the quinol-containing compound, wherein a small peak at ≈ 160 °C indicated the melting temperature of quinol.

All viscosity- and DSC measurements were summarized in Fig. 6e. The areas between expected and measured values were integrated and divided by the area of the respective measurement of CSP1 without additives. Lower values indicate less thermally induced cross-linking, thus higher thermal stability. Since all antioxidant additives were found to work according to the proposed mechanism of a thermally induced cross-linking, the initially developed theoretical framework could once again be verified.

AO1010 performed best, reducing the value of the four cross-linking indicators by 61 % on average. HS3409 also revealed promising results, with a mean reduction of 59 %. The synergistic addition of secondary antioxidants in HS3409 did not lead to an improvement compared to the standalone use of the primary antioxidant AO1010; at least not in the examined concentration. The slightly inferior performance of HS3409 may also be a result of the specific composition of HS3409. This anti-oxidant is tailored to counter the thermal deterioration of styrene-based (co–)polymers. The herein-discussed process however is a result of the specific particle-architecture and not the individual polymer-properties such as the polystyrene-based cores.

Quinol showed the lowest efficiency, but the mean reduction of 37 % was nevertheless an improvement. Quinol and AO1010 are both primary antioxidants, acting as radical scavengers. In direct comparison, it was not surprising that AO1010 showed higher efficiency. It is known that hindering the phenolic hydroxyl group with at least one bulky alkyl group in the ortho position is necessary for high antioxidant activity. The steric hindrance of AO1010 decreases the ability of a phenoxyl radical to abstract a hydrogen atom – in this case from an unconsumed double bond. The long aliphatic chains in AO1010 further improved performance, by decreasing volatility and increasing solubility in the hydrophobic CSP [79].

To investigate a possible influence on self-assembly and thereof resulting color quality, opal films (Figure SI 10) were prepared via application of the melt-shear organization technique at 100 °C. Reflection peaks of additive-containing compounds were slightly red-shifted (Fig. 6f). This indicated that the lattice constant increased. The low-molecular additives seem to have been dispersed in the soft shell matrix, thereby increasing the distance between the core particles. Peak sharpness and perceived color appearance hardly changed upon additive incorporation. Compared to CSP1, the relative reflection intensities were 94 % for HS3409; 96 % for Quinol; and 94 % for AO1010. If there was any influence on the self-assembly of the core particles at all, it must have been minor. We assume, that the low degree of interference with colloidal order was a result of the low weight proportion. Regarding the achievable color quality, the influence of herein investigated additives in a concentration of 2 wt% appears neglectable. This observation is in accordance with the literature, as similar concentrations of several other low-molecular additives have been incorporated in CSP without a deterioration of color quality [26,28,36,55,56,65,72].

Thermal stability may be further improved via optimizations regarding type and dosage of the stabilizer or synergistic combinations with other antioxidants. Nevertheless, the achieved results are very promising. All investigated stabilizers were able to partially suppress or delay thermally induced cross-linking reactions. AO1010 showed the best performance and is thus the most recommended of the three tested additives.

3.6. Combining all Approaches: Overcoming thermal instability

Within the previous chapters, we analytically proved that thermal stability can be increased in several ways. To produce CSP with improved processing stability up to 250 °C, we combined all three solution approaches for batch CSP4. This batch was produced according to the above-described insights comprising particle architecture and anti-oxidant addition. The previously used and examined core batch C3 was used as a starting polymer. As CSP3.1–4 were also based on C3, these batches are well suited for comparison. To achieve an optimized core proportion of 40–45 vol%, we increased the amount of shell-forming monomer during synthesis, compared to CSP3.1–4. The ALMA content inside the interlayer was set to the optimized value of 5 %. Details regarding the synthesis and the recipe are provided in the SI (Table SI 4). After synthesis and freeze drying, 0.03 wt% Carbon Black (as usual) and 2 wt% AO1010 (as an antioxidative additive) were incorporated via microextrusion.

DLS of the particle dispersion (Figure SI 11a) and TEM data (Figure SI 7) confirmed the good control over the polymerization for the formation of CSP4. Compared to CSP3.1–4, a larger particle diameter of $D_{DLS} = 274$ nm (PDI 0.024) and $D_{TEM} = 239$ nm (± 4.3 %) was achieved. This data on particle size was in good agreement with expectations, particularly regarding the core proportion of 41 vol% (according to TEM data). The low PDI and coefficent of variation indicated that mono-disperse particles were obtained. DSC measurements (Figure SI 11b) revealed two glass transitions at –9 °C and 113 °C, thereby proving the formation of a soft shell and rigid core particle architecture, respectively. IR spectra in Figure SI 11c and the corresponding evaluation in Table SI 3 further proved that a higher shell proportion was achieved for CSP4. Compared to CSP3.1, lower intensities of peaks related to the PS cores and higher intensities of peaks related to PEA as shell-polymer were measured. Otherwise, the spectra of CSP4 and CSP3.1 were found to be almost identical, thus proving the good comparability of the synthesized batches.

In analogy to previous analysis, the thermal stability of CSP4 was investigated using rheological examinations and DSC measurements. The batch CSP3.1 was chosen as a comparative particle batch. On the one hand, CSP3.1 resembled the state-of-the-art particle architecture with a common core proportion of 51 vol% (according to TEM data) and the usual ALMA content of 10 wt%. On the other hand, CSP3.1 was based on the same batch of cores as CSP4. Any differences in thermal, rheological, and mechanical properties must therefore be a result of the interlayer composition, core-to-shell ratio, and/or antioxidant incorpo-ration. Fig. 7a and b showed how the viscosity increase of CSP4 was strongly decelerated and overall limited. This observation indicated a restriction of thermally induced cross-linking reactions, as expected and targeted. As mentioned before, DSC analysis in Fig. 7c and d must be interpreted with care, due to potential interfering signals caused by the antioxidant AO1010. The almost fully suppressed exothermic signals in both measurements nevertheless point in the direction of an increased thermal stability. The improved thermal stability was summarized and quantified in Fig. 7e. Compared to the state-of-the-art batch CSP3.1, the lower values of CSP4 demonstrate higher thermal stability in terms of less thermally induced cross-linking. On average, the four cross-linking indicators were reduced by 81 %, thereby proving that thermally induced cross-linking was almost fully suppressed. Moreover, isothermal TGA measurements in N_2 and N_2/O_2 (Figure SI 11d) did not reveal any hints of other thermal deterioration in terms of mass loss.

An opal film was produced to investigate influences on structural color formation by applying the melt-shear technique at 250 °C. The measured reflection spectrum was compared to the previously prepared opal films made of CSP1 and CSP3.1 (Fig. 7f). In case of CSP1 and CSP3.1, melt-shearing was conducted at 100 °C, to avoid thermally induced damage. Both CSP1 and CSP3.1 represented the state-of-the-art particle architecture, but the different sizes of the core particles led to different reflection colors. The red-shift compared to CSP1 and CSP3.1 can be attributed to the larger particle diameter of CSP4 and the additive incorporation, which both led to an increased lattice distance. In terms of peak sharpness and perceived color, the quality of CSP4 was found to be almost identical to the comparative batches. Compared to CSP1, the relative reflection intensity of CSP4 was 95 %, and compared to CSP3.1 even 100 %. It was thus proven, that the structural color quality of CSP4
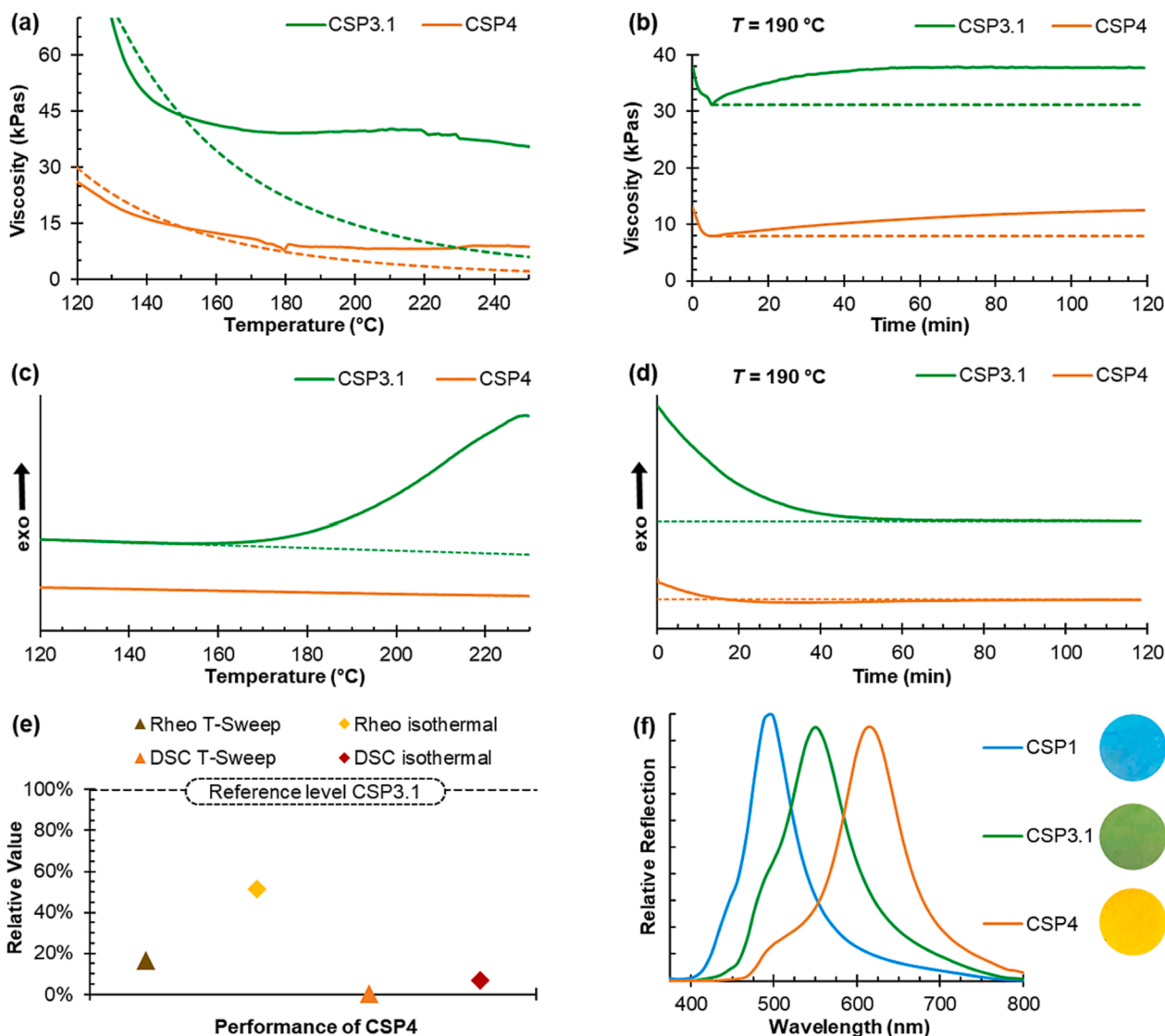
Fig. 7. Comparison of the thermal stability of the optimized batch CSP4 to state-of-the-art particles. **(a)** Temperature-dependent rheological examinations in ambient atmosphere in terms of dynamic complex viscosities. In a temperature range from 35 °C to 165 °C measured viscosities were fitted to Arrhenius-Law and extrapolated for temperatures > 165 °C. **(b)** Isothermal rheological examinations in ambient atmosphere. The minimum viscosity after heating to 190 °C is sketched as a horizontal dotted line. **(c-d)** Temperature-dependent and isothermal DSC measurements in N_2/O_2, wherein the base signals are represented by dotted lines. **(e)** Summary of the measurements. For all four measurements, the area between the expected course and measured values was integrated with respect to the exposition time and normalized in relation to CSP3.1. **(f)** Reflection spectra of opal films, which were prepared via application of the melt-shear technique. The color of the opal film is shown as circles next to the figure legend.

was on a high level, comparable to state-of-the-art particles, and has not been impeded by the undertaken alterations for an increased temperature stability.

As described in the introduction, the rigid cores of CSP-based materials usually self-assemble in the viscous shell-matrix when exhibited to shear-forces during polymer processing and the resulting colloidal crystalline structure gives rise to structural color. To investigate the arrangement of CSP4 after processing, SEM experiments were conducted. The obtained SEM images in Figure SI 12 showed the successful formation of a colloidal crystalline microstructure. The high grade of order can be interpreted as the underlying physical cause for the high quality and intensity of the observed structural color.

3.7. High-Temperature processing and polymer properties

High-temperature processability of CSP4 in comparison of state-of-the-art particles was investigated using microextrusion, melt-shearing,

and 3D printing (Fig. 8). CSP1 and CSP3.1, representing the non-optimized CSP, were found to be non-processable at elevated temperatures. During extrusion at 160–180 °C melt-flow-instabilities were observed, strand breakage occurred, and only short coherent strands with rough surfaces and poor color were obtained. At temperatures above 180 °C the maximum extruder torque was permanently exceeded, even at minimal extrusion speeds. Melt-shearing at 200 °C led to multiple crack formation and an inhomogeneous opal film with poor color quality. The pressed mass turned out to be very brittle, which resulted in crumbling and breaking upon removal of the protective PET foils. 3D printing at 180 °C led to similar results: The material was hardly extrudable, extruded strands were incoherent, color quality was low, and the printed surfaces were rough, inhomogeneous, and crumbly. Moreover, the nozzle clogged after a few layers, forcing it to abort the printing process.

In comparison to these findings, the optimized particle batch CSP4 was conveniently processable at 250 °C. Fig. 8 shows thereof obtained
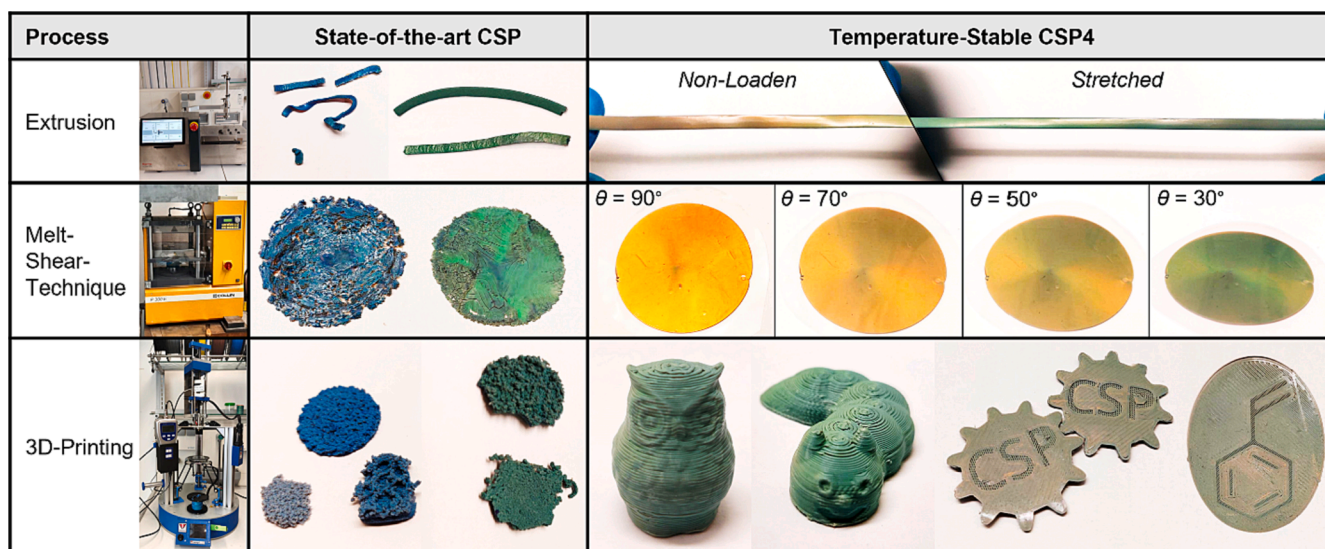
Fig. 8. Comparison of state-of-the-art polymer after high-temperature processing with the optimized batch CSP4 after processing at 250 °C. State-of-the-art particles are represented by CSP1 (left middle column; blue objects) and CSP3.1 (right middle column; green objects). Both show severe signs of thermally induced deterioration. These samples were not used for other purposes in this work, especially not for reflection spectroscopy measurements. Batch CSP4 was extruded into a homogenous strand with a rectangular cross-section of 1x4 mm (top row). Mechanochromic properties are displayed at a strain of 20 %. The angle-dependency of the structural color is demonstrated with an opal film (middle row), which was obtained by application of the melt-shear organization technique and features a diameter of roughly 100 mm. 3D printed objects (bottom row) indicate the obtainable grade of object complexity. The height of the owl is 21 mm; the height of the worm amounts to 12 mm; and the width of the CSP-gears and styrene-ellipse is roughly 40 mm.

structurally colored objects, which featured no signs of deterioration. Regardless of the applied processing technique, color intensity and surface quality were comparable to previously reported materials, which were processed at much lower temperatures [26,27,34,80]. During extrusion, the higher temperature and thus lower viscosity enabled higher material throughput. Compared to extrusion at 150 °C, extrusion speed could be increased by 90 % at 250 °C. Hence, the room-time yield was almost doubled, compared to common CSP processing temperatures. In accordance with Bragg's law of diffraction, the extruded strand was found to be mechanochromic, as it exhibited a color change upon stretching. The appearance of the opal film changed under different viewing angles θ, also according to Bragg's law. This angle dependency is also visible in the 3D printed objects. As they were photographed under a steep angle of $< 30°$, the 3D printed owl and worm appear green. The 3D printed gears and the styrene-slice were photographed under a less steep angle and therefore show more of an orange color. The higher temperature-stability proved to be advantageous in terms of printing speed. Previously reported 3D printable CSP only featured temperature-stability up to 180 °C and were printed at 140 °C with 400 mm min^{-1} [27], while the polymer compound in this work was printed at 250 °C with 600 mm min^{-1}. In other words, it is now possible to produce three owls instead of only two in a given amount of time. The increased printing speed did not reduce printing quality, since all 3D printed objects showed good surface quality as well as a high grade of detail and complexity, featuring a horizontal resolution (layer width) of 0.50 mm and a vertical resolution (layer height) of 0.18 mm.

Besides the above-described advantages for state-of-the-art processing methods, the main target of this work is to enable the cost-effective and wide-spread application of novel processing methods for CSP-based materials, for example injection molding, profile extrusion, all kinds of coating techniques, compression molding, or fused filament fabrication and other commercialized 3D printing techniques. While the application of each single method and the development of CSP with tailored mechanical and rheological properties will be a future work of its own, high temperature stability above 180–200 °C is a prerequisite for almost all of them. High processing temperatures enable steady flow and malleability of the hot material, while the strong viscosity increase upon cooling to

room temperature ensures structural stability and integrity as well as a preservation of the implemented shape.

The potential for practical application of the optimized polymer compound is further enhanced by the possibility of recycling. All produced objects, including the extruded strand, the opal film and the 3D prints can be re-processed. To demonstrate this material property, leftovers from 3D printing and opal film preparation were collected and re-extruded together with the shown extruded strand. The obtained mass was subsequently processed into another opal film via application of the melt-shear technique. Moreover, the 3D printed owl was cut into pieces, loaded into the piston extruder of the 3D printer, and printed into the same owl again. The recycled opal film and owl are shown in Figure SI 13. Both were in no way inferior to the original objects and exhibited comparable surface quality as well as similar structural color. The polymer compounds are not endlessly recyclable though, because at some point all of the antioxidant will be consumed. However, we did not notice such behavior at any point in our experiments, and it can easily be avoided by simply adding an additional portion of antioxidant during the recycling process.

3.8. Advanced Optical, Thermal, and mechanical properties

As described in the introduction, CSP-based materials are in general mechanochromic and goniochromic. This means that they respond to all kinds of mechanical deformation (mechanochromism) as well as alterations of the viewing angle or illumination conditions (goniochromism). Photographs in Fig. 8 already gave a first impression of such stimuli-responsive properties of CSP4. In addition, mechano- and goniochromic reflection spectra of an opal film made of CSP4 are depicted in Fig. 9a and b, respectively. In accordance with Bragg's law, the color of the opal film showed a steady hypsochromic blue-shift at increasing strains and steeper angles, respectively. A strain of 25 % caused a wavelength shift of over 70 nm, whereas a reduction of the angle to 30° led to a shift of roughly 120 nm. In the evaluated strain-range, the mechanochromic response was further found to be reversible, as the original color and reflection intensity were fully recovered, when the test specimen was allowed to relax to the original state. The pronounced
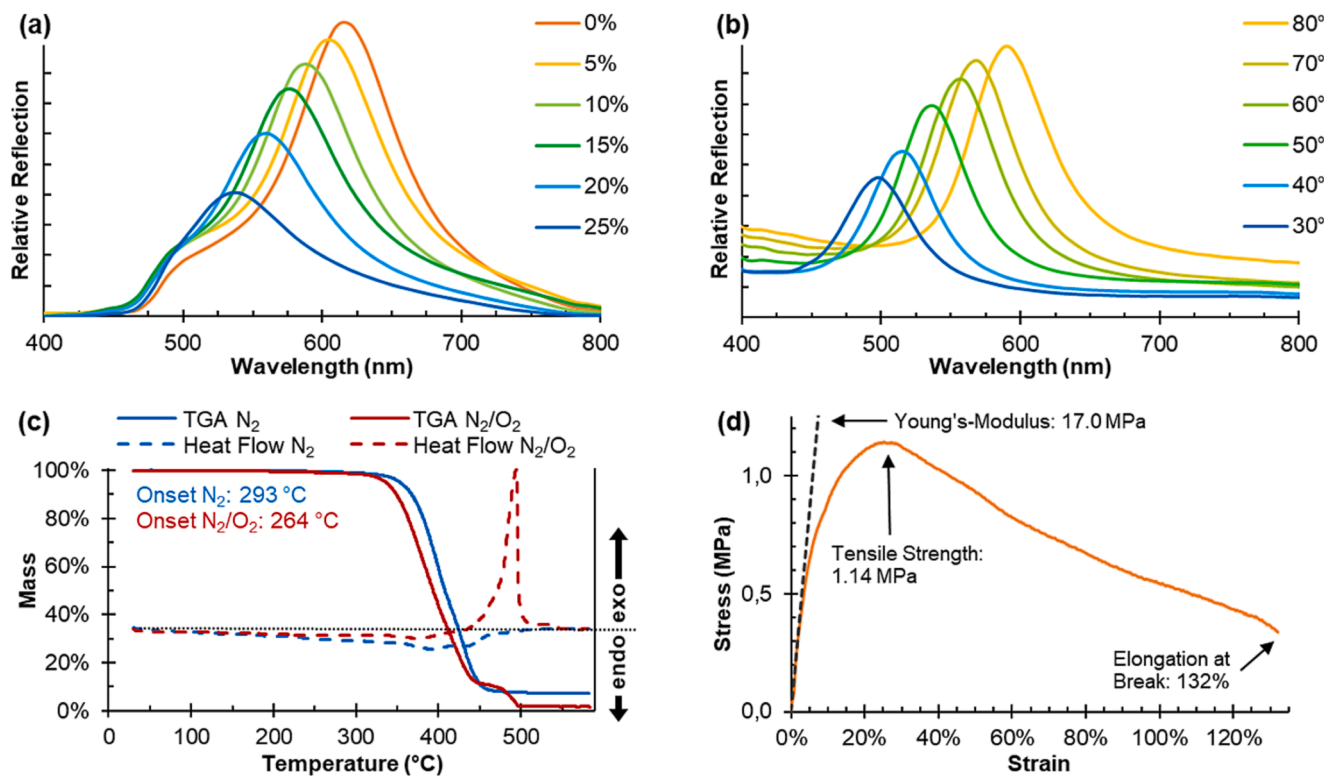
Fig. 9. Optical, thermal, and mechanical properties of the optimized polymer compound CSP4. **(a)** Angle-dependent reflection spectra, illustrating the goniochromic behavior. **(b)** Strain-dependent reflection spectra, illustrating the mechanochromic behavior. **(c)** TGA temperature-sweep in N_2 and N_2/O_2 atmosphere with the corresponding heat flow. **(d)** Tensile test for the determination of mechanical properties.

gonio- and mechanochromic behavior was thus proven, illustrating the stimuli-responsive abilities of the developed material.

Within the previous chapter, it has been shown that for the polymer compound based on CSP4 cross-linking reactions have been efficiently suppressed. While the focus of this work lies on said cross-linking process in a temperature regime $\leq$ 250 °C, TGA temperature sweeps (Fig. 9c) allow for a brief outlook on thermal degradation beyond this temperature range, where other degradation mechanisms must be considered. Since many competitive reactions may occur in this highly complex process, it is beyond the scope of this work, to provide a description of degradation mechanisms or kinetics. Nevertheless, some general observations can be made, which are discussed in the Supporting Information. Within the scope of this work only the maximum temperatures for polymer processing (and application) are of interest. After suppressing the previously limiting cross-linking process and proving the stability of CSP4 at 250 °C, the upper-temperature limit according to TGA may be considered as 250–300 °C, depending on processing technique and temperature holding time.

Besides the previously investigated optical and thermal properties, the mechanical properties are of importance to evaluate practical application potentials. For this purpose, tensile testing of the polymer compound based on CSP4 and AO1010 was conducted (Fig. 9d). The sample showed an elastic-ductile fracture pattern and a high contraction of area in form of necking. The low Young's Modulus of 17.0 MPa and high elongation at break of 132 % reflect the typical properties of a soft elastomer in terms of low stiffness and high stretchability. Given the high proportion of soft PEA shell-polymer (59 vol%), this had to be expected. With the above-described mechanochromic properties, the low stiffness also indicates that low forces are sufficient to trigger deformations which lead to a color shift, thus indicating the suitability for a variety of smart sensing applications. Overall, the mechanical properties of the optimized polymer compound resemble the behavior of a non-covalently cross-linked elastomer, wherein entanglements of shell-

polymer chains act as physical cross-linkers between particles. The rather low tensile strength of 1.14 MPa should not be regarded as a disadvantageous property in general, since the absolute mechanical properties are now conveniently tailorable to the specific application using different advanced processing techniques, for instance by varying object thickness during 3D printing – another decisive advantage, compared to state-of-the-art CSP and state-of-the-art processing options, which are mostly limited to thin films and foils.

4. Conclusion

We discovered why state-of-the-art CSP for structural color materials show surprisingly poor thermal stability: not all grafting anchors are consumed during synthesis and lead to an undesired cross-linking at elevated processing temperatures. Based on this theoretical framework, potential solutions were developed. Temperature stability was found to be improvable via optimizations of the particle architecture, regarding an optimized core proportion of 40–45 vol% and a reduced content of grafting anchor of 5 wt%. Primary antioxidants are well suited to further increase thermal stability, enabling processing temperatures of up to 250 °C. An increased temperature stability generates a variety of advances for established processing methods and may further pave the way for new methods that are not suitable for state-of-the-art CSP. In the case of (micro)extrusion, the lower viscosity at elevated temperatures enables higher throughput and lower engine workload. This is also beneficial for other extrusion-based processes, most prominently injection molding. Regarding the melt-shear technique, higher temperatures facilitate the incorporation of (co–)monomers with relatively high glass transitions in the shell, e.g. all types of methacrylates. Thereby possibilities for the synthesis of CSP and the production of opal films are broadened. The advantages of the melt-shear process also apply to other types of pressing, such as compression molding or coating techniques. In the field of 3D printing, higher temperatures allow for higher printing

speeds and the incorporation of a larger range of monomers. It also reduces the risk of a clogged nozzle and allows for the use of smaller nozzles to achieve higher resolutions. In perspective, temperature-stable CSP could be 3D printed on commercialized printers and with other 3D printing techniques, especially fused filament fabrication. In summary, we envision the developed materials within this work to open new possibilities for the large-scale manufacture of complex 3D objects with tunable and stimuli-responsive structural color. Potential commercial applications range from smart sensors and optical display technologies to decorative effect colors and advanced anti-counterfeiting materials.

Credit authorship contribution statement

Lukas Siegwardt: Conceptualization, Data curation, Formal analysis, Investigation, Methodology, Validation, Visualization, Writing – original draft, Writing – review & editing. **Markus Gallei:** Conceptualization, Data curation, Formal analysis, Funding acquisition, Methodology, Project administration, Resources, Supervision, Validation, Visualization, Writing – original draft, Writing – review & editing.

Declaration of competing interest

The authors declare the following financial interests/personal relationships which may be considered as potential competing interests: Markus Gallei has patent #EP 23210135.2 pending to Saarland University. Lukas Siegwardt has patent #EP 23210135.2 pending to Saarland University.

Data availability

Data will be made available on request.

Acknowledgments

Appendix A. Supplementary data

Supplementary data to this article can be found online at https://doi.org/10.1016/j.cej.2023.148168.

References

[1] S. Yoshioka, S. Kinoshita, Structural or pigmentary? Origin of the distinctive white stripe on the blue wing of a Morpho butterfly, Proc. Biol. Sci. 273 (1583) (2006) 129–134, https://doi.org/10.1098/rspb.2005.3314.

[2] J. Zi, X. Yu, Y. Li, X. Hu, C. Xu, X. Wang, X. Liu, R. Fu, Coloration strategies in peacock feathers, Proc. Natl. Acad. Sci. USA 100 (22) (2003) 12576–12578, https://doi.org/10.1073/pnas.2133313100.

[3] J. Teyssier, S.V. Saenko, D. van der Marel, M.C. Milinkovitch, Photonic crystals cause active colour change in chameleons, Nat. Commun. 6 (2015) 6368, https://doi.org/10.1038/ncomms7368.

[4] O. Kulyk, L. Rocard, L. Maggini, D. Bonifazi, Synthetic strategies tailoring colours in multichromophoric organic nanostructures, Chem. Soc. Rev. 49 (23) (2020) 8400–8424, https://doi.org/10.1039/c9cs00555b.

[5] A.G. Dumanli, T. Savin, Recent advances in the biomimicry of structural colours, Chem. Soc. Rev. 45 (24) (2016) 6698–6724, https://doi.org/10.1039/c6cs00129g.

[6] A.E. Goodling, S. Nagelberg, B. Kaehr, C.H. Meredith, S.I. Cheon, A.P. Saunders, M. Kolle, L.D. Zarzar, Colouration by total internal reflection and interference at microscale concave interfaces, Nature 566 (7745) (2019) 523–527, https://doi.org/10.1038/s41586-019-0946-4.

[7] W. Wang, Y. Zhou, L. Yang, X. Yang, Y. Yao, Y. Meng, B. Tang, Stimulus-responsive photonic crystals for advanced security, Adv. Funct. Mater. 32 (40) (2022), https://doi.org/10.1002/adfm.202204744.

[8] T. Chang, B. Wang, D. Yuan, Y. Wang, I. Smalyukh, G. Zhou, Z. Zhang, Cellulose nanocrystal chiral photonic micro-flakes for multilevel anti-counterfeiting and identification, Chem. Eng. J. 446 (2022), https://doi.org/10.1016/j.cej.2022.136630.

[9] G. Isapour, M. Lattuada, Multiresponsive photonic microspheres formed by hierarchical assembly of colloidal nanogels for colorimetric sensors, ACS Appl. Nano Mater. 4 (4) (2021) 3389–3396, https://doi.org/10.1021/acsanm.0c03150.

[10] Y. Wu, R. Sun, Y. Han, S. Zhang, S. Wu, Ultrathin photonic crystal film with supersensitive thermochromism in air, Chem. Eng. J. 451 (2023), https://doi.org/10.1016/j.cej.2022.139075.

[11] A. Núñez-Montenegro, D.M.A. Crista, J.C.G.E. da Silva, Structural coloration based on photonic crystals for coating applications on wood, Eur. J. Wood. Wood. Prod. 78 (2) (2020) 293–300, https://doi.org/10.1007/s00107-020-01499-9.

[12] L. Shang, W. Zhang, K. Xu, Y. Zhao, Bio-inspired intelligent structural color materials, Mater. Horiz. 6 (5) (2019) 945–958, https://doi.org/10.1039/c9mh00101h.

[13] Z. Cai, Z. Li, S. Ravaine, M. He, Y. Song, Y. Yin, H. Zheng, J. Teng, A. Zhang, From colloidal particles to photonic crystals: advances in self-assembly and their emerging applications, Chem. Soc. Rev. 50 (10) (2021) 5898–5951, https://doi.org/10.1039/d0cs00706d.

[14] J. Ge, Y. Yin, Responsive photonic crystals, Angew. Chem. Int. Ed. Engl. 50 (7) (2011) 1492–1522, https://doi.org/10.1002/anie.200907091.

[15] Y. Hu, D. Yang, D. Ma, S. Huang, Extremely sensitive mechanochromic photonic crystals with broad tuning range of photonic bandgap and fast responsive speed for high-resolution multicolor display applications, Chem. Eng. J. 429 (2022), https://doi.org/10.1016/j.cej.2021.132342.

[16] M. Li, Q. Lyu, B. Peng, X. Chen, L. Zhang, J. Zhu, Bioinspired colloidal photonic composites: fabrications and emerging applications, Adv. Mater. (2022), e2110488, https://doi.org/10.1002/adma.202110488.

[17] Q. Lyu, M. Li, L. Zhang, J. Zhu, Bioinspired supramolecular photonic composites: construction and emerging applications, Macromol. Rapid Commun. 43 (14) (2022), e2100867, https://doi.org/10.1021/jacs.2c02894.

[18] M. Vatankhah-Varnosfaderani, A.N. Keith, Y. Cong, H. Liang, M. Rosenthal, M. Sztucki, C. Clair, S. Magonov, D.A. Ivanov, A.V. Dobrynin, S.S. Sheiko, Chameleon-like elastomers with molecularly encoded strain-adaptive stiffening and coloration, Science 359 (6383) (2018) 1509–1513, https://doi.org/10.1126/science.aar5308.

[19] G. Isapour, M. Lattuada, Bioinspired stimuli-responsive color-changing systems, Adv. Mater. 30 (19) (2018), e1707069, https://doi.org/10.1002/adma.201707069.

[20] L. Schertel, S. Magkiriadou, P. Yazhgur, A. Demirörs, Manufacturing large-scale materials with structural color, Chimia 76 (10) (2022), https://doi.org/10.2533/chimia.2022.833.

[21] K. Li, C. Li, H. Li, M. Li, Y. Song, Designable structural coloration by colloidal particle assembly: from nature to artificial manufacturing, iScience 24 (2) (2021), https://doi.org/10.1016/j.isci.2021.102121.

[22] H. Li, P. Wu, G. Zhao, J. Guo, C. Wang, Fabrication of industrial-level polymer photonic crystal films at ambient temperature Based on uniform core/shell colloidal particles, J. Colloid Interface Sci. 584 (2021) 145–153, https://doi.org/10.1016/j.jcis.2020.09.084.

[23] Q. Yang, W. Ling, Y. Xu, H. Chen, H. Guo, L. Zhong, Y. Qiu, Large-scale production of high-quality elastic structural color films based on hydrogen bond and colloidal charge co-driven silica microsphere self-assembly, Chem. Eng. J. (2022), https://doi.org/10.1016/j.cej.2022.140591.

[24] Z. Zhang, Z. Chen, L. Shang, Y. Zhao, Structural color materials from natural polymers, Adv. Mater. Technol. 6 (11) (2021), https://doi.org/10.1002/admt.202100296.

[25] X. Li, L. Chen, D. Weng, C. Chen, Z. Li, J. Wang, Tension gradient-driven rapid self-assembly method of large-area colloidal crystal film and its application in multifunctional structural color displays, Chem. Eng. J. 427 (2022), https://doi.org/10.1016/j.cej.2021.130658.

[26] M. Gallei, Functional polymer opals and porous materials by shear-induced assembly of tailor-made particles, Macromol. Rapid. Commun. 39 (4) (2018) 1700648, https://doi.org/10.1002/marc.201700648.

[27] L. Siegwardt, M. Gallei, Complex 3D-printed mechanochromic materials with iridescent structural colors based on core-shell particles, Adv. Funct. Mater. 33 (15) (2023), https://doi.org/10.1002/adfm.202213099.

[28] C.G. Schäfer, Stimuli-Responsive Polymer-Opalfilme: Intelligente Materialien für optische Sensoranwendungen und Sicherheitsmerkmale [dissertation], TU Darmstadt, 2016.

[29] V.N. Manoharan, A.B. Stephenson, A field guide to angle-independent structural color, Phys. Today 74 (1) (2021) 62–63, https://doi.org/10.1063/pt.3.4663.

[30] C.E. Finlayson, J.J. Baumberg, Generating bulk-scale ordered optical materials using shear-assembly in viscoelastic media, Materials 10 (7) (2017) 688, https://doi.org/10.3390/ma10070688.

[31] Q. Zhao, C.E. Finlayson, D.R. Snoswell, A. Haines, C.G. Schäfer, P. Spahn, G. P. Hellmann, A.V. Petukhov, L. Herrmann, P. Burdet, P.A. Midgley, S. Butler, M. Mackley, Q. Guo, J.J. Baumberg, Large-scale ordering of nanoparticles using viscoelastic shear processing, Nat. Commun. 7 (2016) 11661, https://doi.org/10.1038/ncomms11661.

[32] T. Ruhl, P. Spahn, G.P. Hellmann, Artificial opals prepared by melt compression, Polymer 44 (25) (2003) 7625–7634, https://doi.org/10.1016/j.polymer.2003.09.047.

[33] O.L.J. Pursiainen, J.J. Baumberg, H. Winkler, B. Viel, P. Spahn, T. Ruhl, Shear-induced organization in flexible polymer opals, Adv. Mater. 20 (8) (2008) 1484–1487, https://doi.org/10.1002/adma.200701363.

[34] C.G. Schäfer, M. Gallei, J.T. Zahn, J. Engelhardt, G.P. Hellmann, M. Rehahn, Reversible light-, thermo-, and mechano-responsive elastomeric polymer opal

films, Chem. Mat. 25 (11) (2013) 2309–2318, https://doi.org/10.1021/cm400911j.

[35] T. Winter, A. Boehm, V. Presser, M. Gallei, Dye-loaded mechanochromic and pH-responsive elastomeric opal films, Macromol. Rapid. Commun. 42 (1) (2021), e2000557, https://doi.org/10.1002/marc.202000557.

[36] O.L.J. Pursiainen, J.J. Baumberg, K. Ryan, J. Bauer, H. Winkler, B. Viel, T. Ruhl, Compact strain-sensitive flexible photonic crystals for sensors, Appl. Phys. Lett. 87 (10) (2005), 101902, https://doi.org/10.1063/1.2032590.

[37] T. Ruhl, P. Spahn, G. Hellmann, H. Winkler, Colloidal crystals from core-shell latex spheres by compression molding, Mesophases, Polymers, and Particles, Springer, Berlin, Heidelberg, 2004, pp. 82-87. https://doi.org/10.1007/b100307.

[38] P. Spahn, C.E. Finlayson, W.M. Etah, D.R.E. Snoswell, J.J. Baumberg, G. P. Hellmann, Modification of the refractive-index contrast in polymer opal films, J. Mater. Chem. 21 (24) (2011) 8893, https://doi.org/10.1039/c1jm00063b.

[39] H. Li, M. Zhu, F. Tian, W. Hua, J. Guo, C. Wang, Polychrome photonic crystal stickers with thermochromic switchable colors for anti-counterfeiting and information encryption, Chem. Eng. J. 426 (2021), https://doi.org/10.1016/j.cej.2021.130683.

[40] K.W. Shah, G.F. Huseien, H.W. Kua, A state-of-the-art review on core-shell pigments nanostructure preparation and test methods, Micro 1 (1) (2021) 55–85, https://doi.org/10.3390/micro1010006.

[41] E. Armstrong, C. O'Dwyer, Artificial opal photonic crystals and inverse opal structures – fundamentals and applications from optics to energy storage, J. Mater. Chem. C 3 (24) (2015) 6109–6143, https://doi.org/10.1039/c5tc01083g.

[42] A.K. Boehm, S. Husmann, M. Besch, O. Janka, V. Presser, M. Gallei, Porous mixed-metal oxide Li-ion battery electrodes by shear-induced co-assembly of precursors and tailored polymer particles, ACS Appl. Mater. Interfaces 13 (51) (2021) 61166–61179, https://doi.org/10.1021/acsami.1c19027.

[43] D. Scheid, C. Lederle, S. Vowinkel, C.G. Schäfer, B. Stühn, M. Gallei, Redox- and mechanochromic response of metallopolymer-based elastomeric colloidal crystal films, J. Mater. Chem. C 2 (14) (2014) 2583, https://doi.org/10.1039/c3tc32525c.

[44] T. Winter, X. Su, T.A. Hatton, M. Gallei, Ferrocene-containing inverse opals by melt-shear organization of core/shell particles, Macromol. Rapid. Commun. 39 (22) (2018) e1800428.

[45] A.K. Boehm, E. Ionescu, M. Koch, M. Gallei, Combining soft polysilazanes with melt-shear organization of core-shell particles: on the road to polymer-templated porous ceramics, Molecules 24 (19) (2019) 3553, https://doi.org/10.3390/molecules24193553.

[46] S. Vowinkel, F. Malz, K. Rode, M. Gallei, Single-source macroporous hybrid materials by melt-shear organization of core–shell particles, J. Mater. Sci. 52 (19) (2017) 11179–11190, https://doi.org/10.1007/s10853-017-0891-2.

[47] C.G. Schäfer, S. Vowinkel, G.P. Hellmann, T. Herdt, C. Contiu, J.J. Schneider, M. Gallei, A polymer based and template-directed approach towards functional multidimensional micro-structured organic/inorganic hybrid materials, J. Mater. Chem. C 2 (37) (2014), https://doi.org/10.1039/c4tc00633j.

[48] R. Xiong, J. Luan, S. Kang, C. Ye, S. Singamaneni, V.V. Tsukruk, Biopolymeric photonic structures: design, fabrication, and emerging applications, Chem. Soc. Rev. 49 (3) (2020) 983–1031, https://doi.org/10.1039/c8cs01007b.

[49] G. von Freymann, V. Kitaev, B.V. Lotsch, G.A. Ozin, Bottom-up assembly of photonic crystals, Chem. Soc. Rev. 42 (7) (2013) 2528–2554, https://doi.org/10.1039/c2cs35309a.

[50] L. Gonzalez-Urbina, K. Baert, B. Kolaric, J. Perez-Moreno, K. Clays, Linear and nonlinear optical properties of colloidal photonic crystals, Chem. Rev. 112 (4) (2012) 2268–2285, https://doi.org/10.1021/cr200063f.

[51] A.P. Hynninen, J.H. Thijssen, E.C. Vermolen, M. Dijkstra, A. van Blaaderen, Self-assembly route for photonic crystals with a bandgap in the visible region, Nat. Mater. 6 (3) (2007) 202–205, https://doi.org/10.1038/nmat1841.

[52] E. Tian, Y. Ma, L. Cui, J. Wang, Y. Song, L. Jiang, Color-oscillating photonic crystal hydrogel, Macromol. Rapid. Commun. 30 (20) (2009) 1719–1724, https://doi.org/10.1002/marc.200900342.

[53] T. Winter, M. Bitsch, F. Müller, S. Voskian, T.A. Hatton, K. Jacobs, V. Presser, M. Gallei, Redox-responsive 2-aminoanthraquinone core-shell particles for structural colors and carbon capture, ACS Appl. Polym. Mater. 3 (9) (2021) 4651–4660, https://doi.org/10.1021/acsapm.1c00746.

[54] Y. Wang, J. Guo, L. Sun, H. Chen, Y. Zhao, Dual-responsive graphene hybrid structural color hydrogels as visually electrical skins, Chem. Eng. J. 415 (2021), https://doi.org/10.1016/j.cej.2021.128978.

[55] Y. Imai, C.E. Finlayson, P. Goldberg-Oppenheimer, Q. Zhao, P. Spahn, D.R. E. Snoswell, A.I. Haines, G.P. Hellmann, J.J. Baumberg, Electrically conductive polymeric photonic crystals, Soft Matter 8 (23) (2012), https://doi.org/10.1039/c2sm06740d.

[56] C.G. Schäfer, C. Lederle, K. Zentel, B. Stuhn, M. Gallei, Utilizing stretch-tunable thermochromic elastomeric opal films as novel reversible switchable photonic

[57] C.G. Schäfer, M. Biesalski, G.P. Hellmann, M. Rehahn, M. Gallei, Paper-supported elastomeric opal films for enhanced and reversible solvatochromic response, J. Nanophotonics 7 (1) (2013), https://doi.org/10.1117/1.Jnp.7.070599.

[58] K.R. Phillips, G.T. England, S. Sunny, E. Shirman, T. Shirman, N. Vogel, J. Aizenberg, A colloidoscope of colloid-based porous materials and their uses, Chem. Soc. Rev. 45 (2) (2016) 281–322, https://doi.org/10.1039/c5cs00533g.

[59] P. Liu, L. Bai, J. Yang, H. Gu, Q. Zhong, Z. Xie, Z. Gu, Self-assembled colloidal arrays for structural color, Nanoscale Adv. 1 (5) (2019) 1672–1685, https://doi.org/10.1039/c8na00328a.

[60] P. Jiang, M.J. McFarland, Large-scale fabrication of wafer-size colloidal crystals, macroporous polymers and nanocomposites by spin-coating, J. Am. Chem. Soc. 126 (42) (2004) 13778–13786, https://doi.org/10.1021/ja0470923.

[61] A. Mihi, M. Ocaña, H. Míguez, Oriented colloidal-crystal thin films by spin-coating microspheres dispersed in volatile media, Adv. Mater. 18 (17) (2006) 2244–2249, https://doi.org/10.1002/adma.200600555.

[62] B. Hatton, L. Mishchenko, S. Davis, K.H. Sandhage, J. Aizenberg, Assembly of large-area, highly ordered, crack-free inverse opal films, Proc. Natl. Acad. Sci. USA 107 (23) (2010) 10354–10359, https://doi.org/10.1073/pnas.1000954107.

[63] C.G. Schäfer, T. Winter, S. Heidt, C. Dietz, T. Ding, J.J. Baumberg, M. Gallei, Smart polymer inverse-opal photonic crystal films by melt-shear organization for hybrid core–shell architectures, J. Mater. Chem. C 3 (10) (2015) 2204–2214, https://doi.org/10.1039/c4tc02788d.

[64] C.E. Finlayson, C. Goddard, E. Papachristodoulou, D.R. Snoswell, A. Kontogeorgos, P. Spahn, G.P. Hellmann, O. Hess, J.J. Baumberg, Ordering in stretch-tunable polymeric opal fibers, Opt. Express 19 (4) (2011) 3144–3154, https://doi.org/10.1364/OE.19.003144.

[65] O.L.J. Pursiainen, J.J. Baumberg, H. Winkler, B. Viel, P. Spahn, T. Ruhl, Nanoparticle-tuned structural color from polymer opals, Opt. Express 15 (15) (2007) 9553–9561, https://doi.org/10.1364/oe.15.009553.

[66] T. Ruhl, Elastomere kolloidale Kristalle aus hart-weichen Kern-Mantel-Latices [dissertation], Fachbereich Chemie, TU Darmstadt, Darmstadt, 2003.

[67] F.N. Cogswell, Polymer melt rheology: a guide for industrial practice, Woodhead Publishing Limited, Cambridge, England, 2003.

[68] Z. Tadmor, C.G. Gogos, Principles of Polymer Processing, 2 ed., John Wiley & Sons, New York, 2008.

[69] C.E. Finlayson, G. Rosetta, J.J. Baumberg, An experimental and theoretical determination of oscillatory shear-induced crystallization processes in viscoelastic photonic crystal media, Materials 14 (18) (2021) 5298, https://doi.org/10.3390/ma14185298.

[70] H.S. Wong, M. Mackley, S. Butler, J. Baumberg, D. Snoswell, C. Finlayson, Q. Zhao, The rheology and processing of "edge sheared" colloidal polymer opals, J. Rheol. 58 (2) (2014) 397–409, https://doi.org/10.1122/1.4862920.

[71] C.E. Finlayson, P. Spahn, D.R. Snoswell, G. Yates, A. Kontogeorgos, A.I. Haines, G. P. Hellmann, J.J. Baumberg, 3D bulk ordering in macroscopic solid opaline films by edge-induced rotational shearing, Adv. Mater. 23 (13) (2011) 1540–1544, https://doi.org/10.1002/adma.201003934.

[72] C.G. Schäfer, B. Viel, G.P. Hellmann, M. Rehahn, M. Gallei, Thermo-cross-linked elastomeric opal films, ACS Appl. Mater. Interfaces 5 (21) (2013) 10623–10632, https://doi.org/10.1021/am402588v.

[73] G. Schmidt-Naake, B. Bulmahn, G. Janke, B. Witt, Copolymere aus bifunktionellen Vinylmonomeren: Allylmethacrylat mit Methylmethacrylat und Styrol, Angew. Makromol. Chem. 248 (1) (2003) 23–40, https://doi.org/10.1002/apmc.1997.052480102.

[74] G. Rosetta, T. An, Q. Zhao, J.J. Baumberg, J.J. Tomes, M.D. Gunn, C.E. Finlayson, Chromaticity of structural color in polymer thin film photonic crystals, Opt. Express. 28 (24) (2020) 36219–36228, https://doi.org/10.1364/OE.410338.

[75] C.E. Finlayson, G. Rosetta, J.J. Tomes, Spectroscopic ellipsometry and optical modelling of structurally colored opaline thin-films, Appl. Sci. 12 (10) (2022), https://doi.org/10.3390/app12104888.

[76] D.R. Snoswell, A. Kontogeorgos, J.J. Baumberg, T.D. Lord, M.R. Mackley, P. Spahn, G.P. Hellmann, Shear ordering in polymer photonic crystals, Phys. Rev. e. Stat. Nonlin. Soft Matter Phys. 81 (2 Pt 1) (2010), 020401, https://doi.org/10.1103/PhysRevE.81.020401.

[77] J. Brandrup, E.H. Immergut, E.A. Grulke, Polymer Handbook, John Wiley & Sons, New York, 1999.

[78] B. Halliwell, How to characterize an antioxidant: an update, Biochem. Soc. Symp. 61 (1995) 73–101, https://doi.org/10.1042/bss0610073.

[79] T. Richard, Antioxidants, Polymers, in: C. Ley (Ed.), Kirk-Othmer Encyclopedia of Chemical Technology, John Wiley & Sons, 2000, pp. 102–134.

[80] C.E. Finlayson, J.J. Baumberg, Polymer opals as novel photonic materials, Polym. Int. 62 (10) (2013) 1403–1407, https://doi.org/10.1002/pi.4582.